THE ASTROPHYSICAL JOURNAL, 509:861–878, 1998 December 20

RADIO EMISSION AND PARTICLE ACCELERATION IN SN 1993J

CLAES FRANSSON[1] AND CLAES-INGVAR BJÖRNSSON[1]
Received 1998 April 27; accepted 1998 July 27

ABSTRACT

The radio light curves of SN 1993J are discussed. We find that a fit to the individual spectra by a synchrotron spectrum, suppressed by external free-free absorption and synchrotron self-absorption, gives a superior fit to models based on pure free-free absorption. A standard r^{-2} circumstellar medium is assumed and is found to be adequate. From the flux and cutoff wavelength, the magnetic field in the synchrotron-emitting region behind the shock is determined to $B \approx 64(R_s/10^{15}\ \mathrm{cm})^{-1}$ G. The strength of the field argues strongly for turbulent amplification behind the shock. The ratio of the magnetic and thermal energy density behind the shock is ~ 0.14. Synchrotron losses dominate the cooling of the electrons, whereas inverse Compton losses due to photospheric photons are less important. For most of the time also Coulomb cooling affects the spectrum. A model where a constant fraction of the shocked, thermal electrons are injected and accelerated, and subsequently lose their energy due to synchrotron losses, reproduces the observed evolution of the flux and number of relativistic electrons well. The injected electron spectrum has $dn/d\gamma \propto \gamma^{-2.1}$, consistent with diffusive shock acceleration. The injected number density of relativistic electrons scales with the thermal electron energy density, ρV^2, rather than the density, ρ. The evolution of the flux is strongly connected to the deceleration of the shock wave. The total energy density of the relativistic electrons, if extrapolated to $\gamma \sim 1$, is $\sim 5 \times 10^{-4}$ of the thermal energy density. The free-free absorption required is consistent with previous calculations of the circumstellar temperature of SN 1993J, $T_e \sim (2\text{–}10) \times 10^5$ K, which failed in explaining the radio light curves by pure free-free absorption. Implications for the injection of the relativistic electrons, and the relative importance of free-free absorption, Razin suppression, and the synchrotron self-absorption effect for other supernovae, are also briefly discussed. It is argued that especially the expansion velocity, both directly and through the temperature, is important for determining the relative importance of the free-free absorption and synchrotron self-absorption. Some guidelines for the modeling and interpretation of VLBI observations are also given.

Subject headings: acceleration of particles — radiation mechanisms: nonthermal — supernovae: individual (SN 1993J)

1. INTRODUCTION

The radio emission from a young supernova provides an important probe of the circumstellar environment of the supernova (Chevalier 1990; Fransson 1994). In addition, the time dependence of the physical conditions makes it a unique laboratory for studies of relativistic particle acceleration.

For the first radio supernovae to be well observed, SN 1979C and SN 1980K (Weiler et al. 1986), a standard model to explain their radio light curves was soon developed (Chevalier 1982b). The basic feature of this model is external free-free absorption in a circumstellar medium of the synchrotron emission, arising close to the supernova shock wave. Because of the expansion, the optical depth decreases as $\tau_{\rm ff} \propto \lambda^2 R_s^{-3} \propto \lambda^2 t^{-3}$, if the shock velocity is constant. The intrinsic emission from the shock, i.e., the injection efficiency of relativistic particles, as well as the magnetic field, were assumed to scale with the thermal energy density behind the shock. This and alternative scalings have been discussed by Chevalier (1996). This model has been successful in explaining the observations of "standard" Type IIs (Chevalier 1984), and with a knowledge of the temperature, the mass-loss rate of the progenitor can be determined. Calculations of the temperature (Lundqvist & Fransson 1988) show that $T_e \approx 10^5$–10^6 K, and mass-loss rates of 3×10^{-5} and $1.2 \times 10^{-4}\ M_\odot\ \mathrm{yr}^{-1}$ were derived for SN 1980K and SN 1979C, respectively. The model has since been applied to a number of other supernovae, although the observational data for most of these have been less complete.

With the recent Type IIb SN 1993J the most complete data set of any supernova has become available (Van Dyk et al. 1994; Pooley & Green 1993). When the free-free absorption model was applied to this, however, it was found that only a poor fit was obtained (Lundqvist 1994; Fransson, Lundqvist, & Chevalier 1996, hereafter FLC96; Van Dyk et al. 1994). An improved, although still unsatisfactory, fit was obtained if the external density followed $\rho \propto r^{-d}$ instead of $\rho \propto r^{-2}$, where $d = 1.5$–1.7. The reason for this flatter profile was not clear, although speculations about variations in the mass loss rate have been proposed. Not surprisingly, even more complex models could improve the fit, but at the expense of a larger number of free parameters without obvious physical meaning. A serious problem, pointed out by FLC96, was that the temperature in the circumstellar medium was $\gtrsim 2 \times 10^5$ K, resulting in a much smaller free-free optical depth than necessary to produce the required absorption.

In this paper we discuss alternative explanations to the free-free absorption model and show that the radio spectra of SN 1993J are very well explained by a combination of synchrotron self-absorption and external free-free absorption, explaining the anomalous behavior of SN 1993J, as compared with other radio supernovae. Synchrotron self-

[1] Stockholm Observatory, SE-133 36 Saltsjöbaden, Sweden; claes@astro.su.se, bjornsson@astro.su.se.

absorption has been proposed to be responsible for the low-frequency cutoff in Type Ib supernovae (Shklovskii 1985; Slysh 1990) and has been discussed independently from the present analysis by Chevalier (1998). Chevalier & Dwarkadas (1995) have proposed that the turn on of the early radio emission of SN 1987A was determined by synchrotron self-absorption. Several of the mechanisms below were discussed by Chevalier (1982b), who, however, for good reasons discarded them for SN 1979C and SN 1980K.

In § 2 we discuss the synchrotron emissivity at a finite density of thermal electrons, including the Razin-Tsytovich effect, and in § 3 we apply this analysis to the spectra of SN 1993J. First we use simple parameterized models with constant spectral index and discuss the resulting fits for models with the three different suppression mechanisms, i.e., free-free absorption, synchrotron self-absorption, and the Razin-Tsytovich effect. After this we discuss a self-consistent model where the spectral index is determined by the various energy-loss mechanisms. In § 4 we then discuss the results of this analysis, and their implications for the magnetic field, relativistic particle acceleration, and circumstellar temperature. Section 5 contains models for the full light curves, while in § 6 we discuss the relative importance of the Razin-Tsytovich effect, synchrotron self-absorption, and free-free absorption. In § 7 we make some comments on the analysis of VLBI observations of supernovae. The conclusions are summarized in § 8.

2. ABSORPTION AND SUPPRESSION MECHANISMS FOR THE SYNCHROTRON EMISSION

A main advantage in analyzing the individual radio spectra for the various observed dates is that they are only a function of the spectral index of the synchrotron emission, the normalization of the spectrum, and a one-parameter or at most two-parameter specified function, describing the effect of the external or emitting medium. In contrast, an analysis based on the light curves of the different wavelength bands involves uncertain assumptions about the particle acceleration mechanism (e.g., Chevalier 1996). From the time variation of the parameters involved in the fitting of the individual spectra, we can instead hope to gain some understanding of these uncertain, but extremely important, properties of the particle acceleration.

For a homogeneous shell with a synchrotron optical depth $\tau_s(t)$, and with an external free-free medium, parameterized by the optical depth $\tau_{\rm ff}(t)$ at a wavelength $\lambda = 1$ cm, Gaunt factor $g_{\rm ff}(\lambda)$, and impact parameter s, the spectrum is given by

$$F_\nu(\lambda) = 2\pi\left(\frac{R_s}{D}\right)^2 S_\nu \int_0^1 (1 - e^{-\tau_s(s,t)}) e^{-\tau_{\rm ff}(s,t) g_{\rm ff}(\lambda)\lambda^2} s\, ds\,, \quad (1)$$

where

$$\tau_s(s, t) = \frac{\tau_s(0, t)}{(1 - s^2)^{1/2}}\,, \quad (2)$$

$$\tau_{\rm ff}(s, t) = \int_{R_s}^\infty \frac{\kappa_{\rm ff}(r) n_e(r)^2 r}{(r^2 - s^2 R_s^2)^{1/2}}\, dr\,. \quad (3)$$

Here, $\kappa_{\rm ff}$ is the free-free opacity at 1 cm and n_e is the thermal electron density. S_ν is the source function, $S_\nu = j_\nu/\kappa_\nu$, with κ_ν the synchrotron self-absorption opacity and j_ν the emissivity. Finally, R_s and D are the radius of the emitting shell and the distance to the supernova, respectively. We assume that the supernova ejecta are opaque to the radio emission, as is most likely the case.

In the analysis in § 3.1.1, we assume that the column density of electrons have a constant power law, giving a synchrotron spectrum with index α. If we further replace equation (1) by an average over the disk, we then get

$$F_\nu(\lambda) = S'(t)\lambda^{-5/2}(1 - e^{-\bar\tau_s(t)\lambda^{(\alpha+5/2)}}) e^{-\bar\tau_{\rm ff}(t) g_{\rm ff}(\lambda)\lambda^2}\,, \quad (4)$$

where the parameter $S'(t)$ is related to S_ν at 1 cm by $S' = \pi R_s^2\, S_\nu(1\ {\rm cm})/D^2$. The average optical depth over the disk, $\bar\tau_s$, is given by $\bar\tau_s \approx 2\kappa_s \Delta R_{\rm em}$, where $\Delta R_{\rm em}$ is the thickness of the emitting shell. In the optically thin limit, we have

$$F_\nu(\lambda) \approx 2\pi\left(\frac{R_s}{D}\right)^2 j_\nu(t)\Delta R_{\rm em}\, e^{-\bar\tau_{\rm ff}(t) g_{\rm ff}(\lambda)\lambda^2}\,. \quad (5)$$

In the general case of a plasma with density n_e, magnetic field B, and relativistic electron distribution $N(\gamma)$ (integrated along the line of sight and assumed to have an isotropic pitch angle distribution), the line-of-sight integrated emissivity is given by (Tsytovich 1951; Razin 1960; Pacholczyk 1970)

$$j_\nu \Delta R_{\rm em} = 1.87 \times 10^{-23} B \sin\theta \int_1^\infty N(\gamma) f\left(\frac{\nu_p \gamma}{\nu}\right) \times F\left[\frac{\nu}{\nu_{\rm c} f(\nu_p\gamma/\nu)^3}\right] d\gamma\,, \quad (6)$$

where θ is the pitch angle, $\nu_p = 8.98 \times 10^3 n_e^{1/2}$ Hz is the plasma frequency, and $\nu_{\rm c} = \nu_0\, B \sin\theta\gamma^2$ is the critical frequency, where $\nu_0 = 4.20 \times 10^6$ Hz. $F(x)$ is given by

$$F(x) = x \int_x^\infty K_{5/3}(z) dz\,, \quad (7)$$

where $K_{5/3}(z)$ is the modified Bessel function of order 5/3. The function $f(x) = (1 + x^2)^{-1/2}$ represents the modification due to plasma effects. Similarly, the synchrotron self-absorption optical depth is given by

$$\tau_\nu = 1.02 \times 10^4 \frac{B \sin\theta}{\nu^2} \int_1^\infty \gamma^2 \frac{d}{d\gamma}\left[\gamma^{-2} N(\gamma)\right] \times f\left(\frac{\nu_p\gamma}{\nu}\right) F\left[\frac{\nu}{\nu_{\rm c} f(\nu_p\gamma/\nu)^3}\right] d\gamma\,. \quad (8)$$

For a constant power-law distribution of electrons, $N(\gamma) \equiv N_{\rm rel}\,\gamma^{-p}$, one finds

$$j_\nu \Delta R_{\rm em} = 9.33 \times 10^{-24} (1.40 \times 10^{-4}\lambda)^\alpha \times (B \sin\theta)^{(\alpha+1)} N_{\rm rel} \int_0^\infty g(x) F\left[\frac{x}{g(x)^3}\right] x^{(\alpha-1)} dx\,, \quad (9)$$

where

$$g(x) \equiv \left(1 + \frac{\lambda}{\lambda_{\rm R}\, x}\right)^{-1/2} \quad (10)$$

and $\alpha = (p - 1)/2$. The critical wavelength, $\lambda_{\rm R}$, above which the emission is suppressed is given by

$$\lambda_{\rm R} = \frac{3}{4}\frac{B \sin\theta}{e n_e} = \left(\frac{n_e}{1.56 \times 10^9\ {\rm cm}^{-3}}\right)^{-1} B \sin\theta\ {\rm cm}\,. \quad (11)$$

Equation (6) contains the pitch angle between the magnetic field and the electron velocity. Microscopically, the

magnetic field may be random because of turbulence behind the shock. In the integrated flux, as measured by the Very Large Array (VLA), one observes a well-ordered field even from different directions, because of the spherical geometry of the shock. We therefore average equation (6) over all angles numerically. We also assume that the magnetic field and density are constant over the emitting volume. Furthermore, to isolate the wavelength dependence from the variation in the normalization, we split the flux into one wavelength-independent amplitude, $A(t)$, and one spectral function, $P(\lambda/\lambda_{R0}, \alpha)$,

$$F_\nu(\lambda) = A(t)P(\lambda/\lambda_{R0}, \alpha) . \quad (12)$$

Here

$$A(t) = 5.86 \times 10^{-23}\left(\frac{n_e}{2.19 \times 10^5 \text{ cm}^{-3}}\right)^{-\alpha} B^{2\alpha+1} N_{\text{rel}}\left(\frac{R_s}{D}\right)^2 \quad (13)$$

and $\lambda_{R0} = \lambda_R(\theta = \pi/2)$. The spectral function $P(y, \alpha)$ is given by

$$P(y, \alpha) = \frac{y^\alpha}{2}\int_0^\pi \sin\theta^{(\alpha+1)} \int_0^\infty \left(1 + \frac{y}{x \sin\theta}\right)^{-1/2} \times F\left[x\left(1 + \frac{y}{x \sin\theta}\right)^{3/2}\right] x^{(\alpha-1)} dx\, d\cos\theta ; \quad (14)$$

$P(y, \alpha)$ is shown in Figure 1 for several values of α. The averaged and nonaveraged spectra differ only marginally from each other. The averaged spectrum has a slightly shallower slope close to the maximum.

At wavelengths longer than λ_{R0}, the emission is severely suppressed. This effect has been referred to as alternatively the Razin-Tsytovich effect or simply the Razin effect. In the following we will for simplicity use the latter terminology. The vacuum case is obtained for $\lambda_{R0} \to \infty$ when $f = 1$. For wavelengths longer than λ_{R0}, the pitch angle–averaged spectrum falls off as

$$F_\nu \propto N_{\text{rel}} B^{\alpha+1} \lambda^\alpha \left(\frac{\lambda}{\lambda_{R0}}\right)^{(\alpha-1/2)} e^{-(3^{3/2}/2^{1/2})(\lambda/\lambda_{R0})} \quad (15)$$

(Simon 1969). The cutoff due to the Razin effect is therefore less steep than that due to free-free absorption. This is important for the shape of the spectrum at long wavelengths.

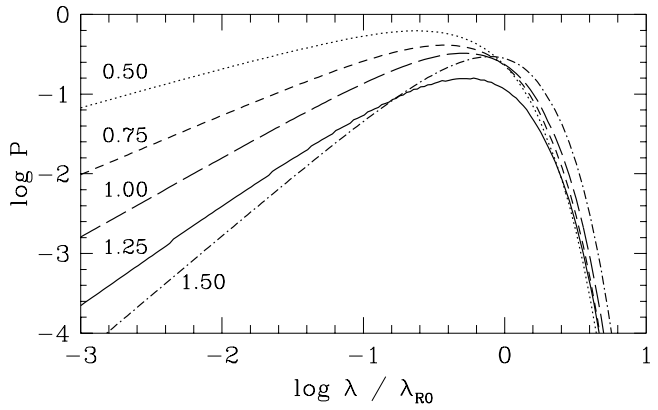

FIG. 1.—Angle-averaged synchrotron spectra, including the Razin effect, for different power-law indices, α. The Razin wavelength is given by $\lambda_{R0} = 1.56 \times 10^9 B/n_e$ cm.

The relevant values of n_e and B depend on the particle acceleration site. If this is in the shocked circumstellar gas, n_e will be a factor of 4 higher than the electron density in the wind. In FLC96 and Fransson (1998) the X-ray emission of SN 1993J at early and late times is modeled. To reproduce the observed X-ray flux, a mass-loss rate of $\dot{M} \approx 5 \times 10^{-5}$ $M_\odot$ yr^{-1} is required, for a wind velocity of $u_w = 10$ km s^{-1}. With a factor of 4 compression, and $X(\text{He})/X(\text{H}) = 0.3$ (e.g., Shigeyama et al. 1994), the electron density immediately behind the circumstellar shock is

$$n_e = 4.36 \times 10^8 \dot{\mathcal{M}}\left(\frac{R_s}{10^{15} \text{ cm}}\right)^{-2} = 1.46 \times 10^8 \dot{\mathcal{M}}\left(\frac{V}{2 \times 10^4 \text{ km s}^{-1}}\right)^{-2} \times \left(\frac{t}{10 \text{ days}}\right)^{-2} \text{cm}^{-3} . \quad (16)$$

The similarity solution by Chevalier (1982a) shows that the density behind the circumstellar shock is fairly constant (see also Fig. 3 in FLC96), and we will use equation (16) throughout the shocked region. We have here for future convenience defined a normalized mass loss, $\dot{\mathcal{M}}$, rate by

$$\dot{\mathcal{M}} \equiv \left(\frac{\dot{M}}{5 \times 10^{-5} M_\odot \text{ yr}^{-1}}\right)\left(\frac{u_w}{10 \text{ km s}^{-1}}\right)^{-1} . \quad (17)$$

In FLC96 it is argued that $V \approx 2 \times 10^4$ km s^{-1} at $\sim$10 days. VLBI observations (Marcaide et al. 1995a, 1995b, 1997; Bartel et al. 1994) give an expansion velocity for the radio-emitting plasma of $\sim(1.8–2.4) \times 10^4$ km s^{-1} during the first $\sim$100 days. Consequently, we scale our results to $V = 2 \times 10^4$ km s^{-1}. The motivation for this and the evolution of the velocity is discussed further in § 3.2.3.

With this density, λ_{R0} is given by

$$\lambda_{R0} = 10.7 \dot{\mathcal{M}}\left(\frac{B}{1 \text{ G}}\right)\left(\frac{V}{2 \times 10^4 \text{ km s}^{-1}}\right)^2\left(\frac{t}{10 \text{ days}}\right)^2 \text{cm} . \quad (18)$$

The magnetic field in the emitting region therefore has to be less than $\sim$1 G, or alternatively, $\dot{M}/u_w$ large, for the Razin effect to be important.

3. APPLICATION TO SN 1993J

Although radio observations are available for a large number of supernovae (e.g., Weiler et al. 1998 for a review), SN 1993J is unique in terms of the frequency of observations, small errors in the observed fluxes, and the large wavelength coverage. It is therefore by far the object best suited for a detailed analysis. Observations have been published by Van Dyk et al. (1994) and Weiler et al. (1998) for 1.33–21 cm from 5 to 1300 days and by Pooley & Green (1993) at 2 cm from 8 to 114 days. In addition, there is one set of VLA observations at 923 days for 1.3–90 cm (Montes et al. 1995). A few millimeter observations with IRAM and OVRO also exist (Radford 1993; Phillips & Kulkarni 1993a, 1993b). The fluxes of the millimeter observations do, however, not agree at similar epochs, and it is difficult to judge the accuracy of these observations. For the modeling of the spectra in this paper, we use the VLA observations by

Van Dyk et al. and Weiler et al., as well as the day 923 observation by Montes et al. In § 5 we also include the Ryle telescope observations by Pooley & Green (1993), as well as the VLA dates having only a partial spectral coverage, in particular, before ~ 10 days.

Our strategy is first to investigate the simplest models, based on a pure power-law electron and synchrotron spectrum, studying one suppression mechanism at a time. By analyzing the results of this, in particular, the consistency of these models, we test their validity as well as explore the likely range of the relevant physical parameters, in particular, the magnetic field. However, as a result of the failure of these simple models we are in § 3.2 led to a more detailed analysis, taking all the relevant physical processes into account.

3.1. *Constant Spectral Index Fits*

3.1.1. *One-Component Models*

We will now use equation (4), assuming here a constant spectral index $\alpha = (p-1)/2$, in the three limiting cases: (1) free-free absorption, $\tau_s = 0$, $\tau_{\rm ff} \neq 0$, $\lambda \ll \lambda_{\rm R0}$; (2) synchrotron-self absorption, $\tau_s \neq 0$, $\tau_{\rm ff} = 0$, $\lambda \ll \lambda_{\rm R0}$; (3) Razin suppression, $\tau_s = 0$, $\tau_{\rm ff} = 0$, $\lambda \approx \lambda_{\rm R0}$. In the free-free and Razin cases we use the optically thin expression, equation (5). In all three cases there are three parameters characterizing the spectrum: (1) the overall normalization of the synchrotron spectrum; (2) the power-law index of the radiation (α); (3) the optical depth to free-free absorption ($\tau_{\rm ff}$), synchrotron self-absorption (τ_s), or the Razin cutoff wavelength ($\lambda_{\rm R0}$). For each date we fit the observed spectrum with the set of parameters that minimizes χ^2. The value of α is determined by minimizing the scatter of the overall light curves; in the Razin case, especially the spectral region where $\lambda \ll \lambda_{\rm R0}$, and for the free-free and synchrotron self-absorption cases the spectral region where $\tau(\lambda) \ll 1$. As we discuss below, there are reasons to expect that, because of cooling, α varies with time and frequency. This will be discussed in detail in § 5.

In Figure 2 we show the observed fluxes at 1.3, 2.0, 3.6, 6.2, and 21 cm at 11.5, 22.3, 40.1, and 75.1 days. These dates were picked to cover well the exponentially damped part of the spectrum. The solid line represents the best fit Razin spectrum, while the dashed line is the best-fit free-free absorption spectrum, and the dotted line shows the same

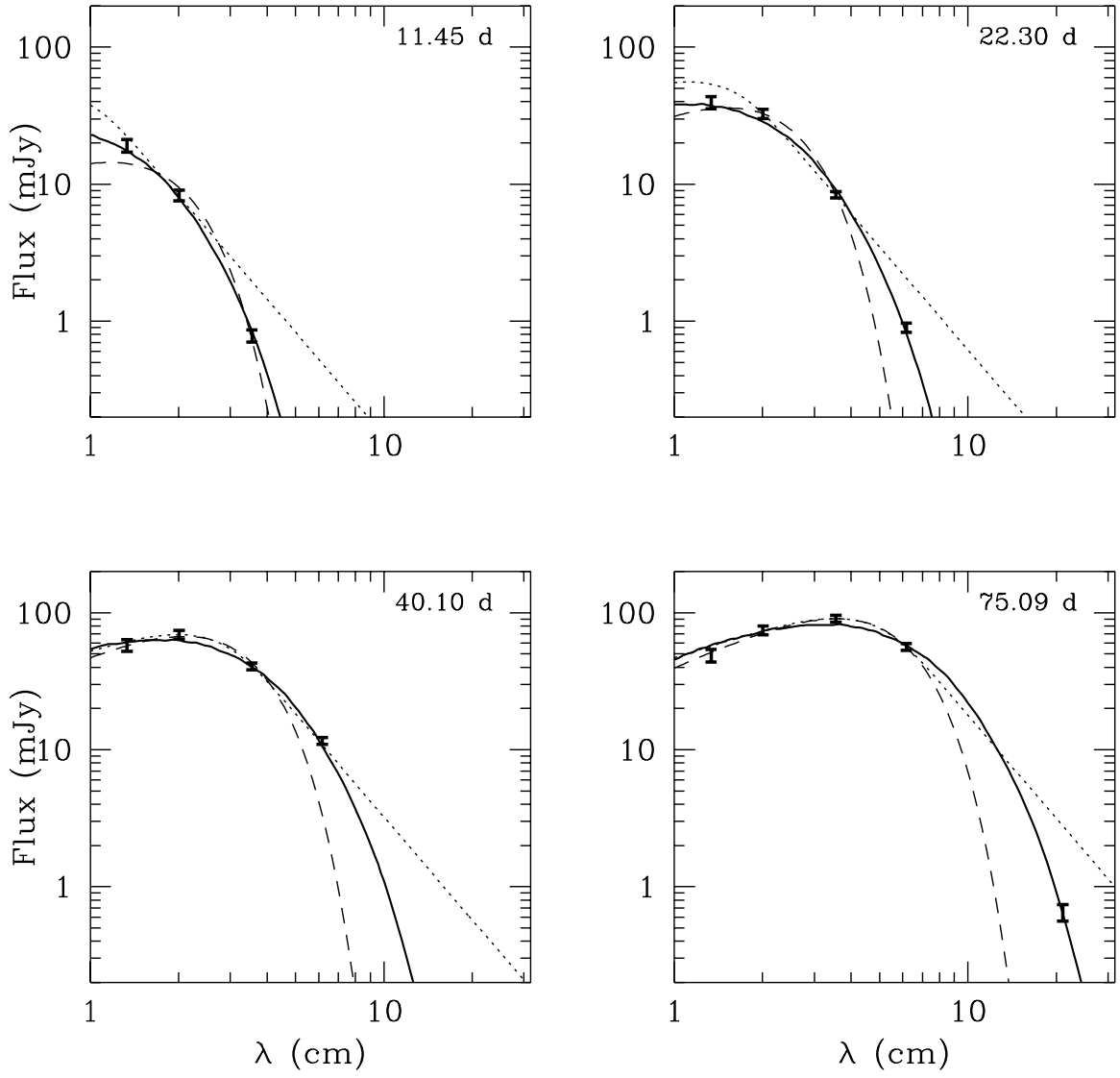

FIG. 2.—Observed VLA spectra at four epochs, from Van Dyk et al. (1994), together with fits based on a Razin-suppressed synchrotron spectrum (*solid line*), external free-free absorption (*dashed line*), and synchrotron self-absorption (*dotted line*).

for the synchrotron self-absorption case. In the Razin case, $\alpha = 1.25 \pm 0.1$ gives the best fit. In the free-free case, $\alpha = 0.8$ is indicated, while the best fit in the synchrotron self-absorption case is obtained for $\alpha = 0.7$. The reason for this difference in α is that the Razin effect affects the spectrum well below λ_{R0} and flattens the overall spectrum. The free-free absorption sets in more abruptly and has less of an effect at short wavelengths (cf. eqs. [5] and [15]).

From Figure 2 it is obvious that the Razin spectrum gives a superior fit to the observations compared with free-free or synchrotron self-absorption. Only when all wavelengths are close to the nonsuppressed level, as at 40.1 days, do free-free and synchrotron self-absorption provide acceptable fits. Otherwise the free-free spectrum underestimates the flux, while the synchrotron self-absorption overestimates above the wavelength cutoff. At $t \gtrsim 200$ days, all models give reasonable fits because of the decreasing importance of the Razin effect, synchrotron self-absorption, and free-free absorption at $\lambda \lesssim 20$ cm.

Because the Razin fit provides the best one-component fit, we now analyze the implications and consistency of this model in more detail. We have therefore calculated the best fit for all dates that have enough frequency points (three for $t < 16$ days, four for $16 < t < 75$ days, and five for 75 days $< t$). The Razin wavelength, λ_{R0}, and the normalization parameter $A(t)$ (in mJy) (see eq. [12]) are calculated for these dates and shown in Figure 3. During the whole period the Razin wavelength shows a very smooth evolution. The solid line in Figure 3 shows a simple power-law fit to the evolution, determined by a least-squares fit. Using

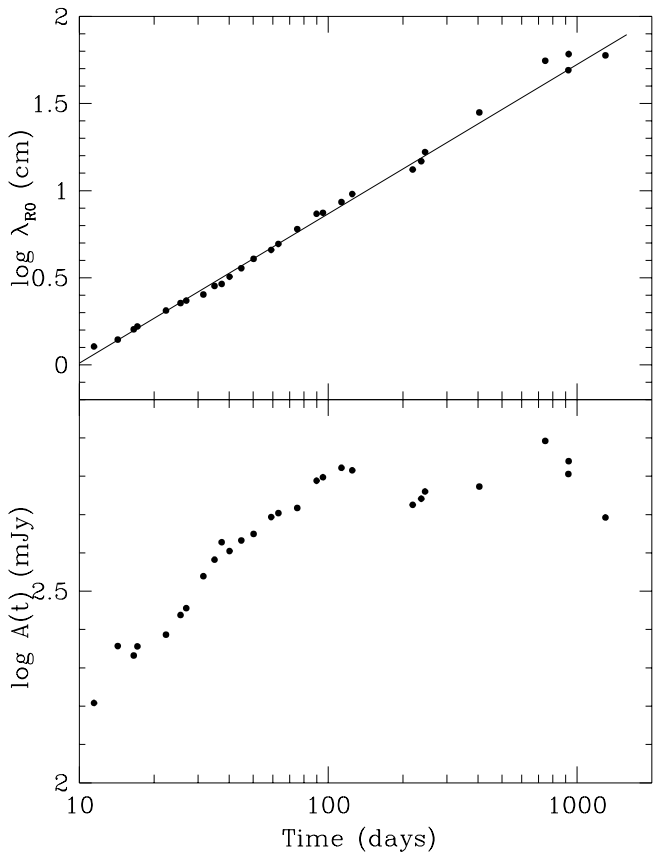

FIG. 3.—Derived values of $\lambda_{R0} \propto B/n_e$ and $A(t)$ from the fits to the Razin model. The solid line gives a best linear fit to the log B/n_e vs. log t relation.

equation (11), the ratio B/n_e can be fit with the function

$$\frac{B}{n_e} = 6.6 \times 10^{-10}\left(\frac{t}{10 \text{ days}}\right)^{0.86} \tag{19}$$

with an rms of only ± 0.013 in the exponent. Inserting equation (16) into equation (19), the magnetic field can be obtained for the same region as a function of time:

$$B \approx 9.6 \times 10^{-2} \dot{M}\left(\frac{V}{2 \times 10^4 \text{ km s}^{-1}}\right)^{-2}\left(\frac{t}{10 \text{ days}}\right)^{-1.14} \text{G} . \tag{20}$$

To calculate the total number of relativistic electrons we eliminate in equations (12) and (13) the magnetic field and electron density by using equations (20) and (16) and find with $p = 3.5$

$$F_\nu = 1.14 \times 10^{-23} \dot{M}^{2.25}\left(\frac{V}{2 \times 10^4 \text{ km s}^{-1}}\right)^{-2.5} N_{\text{rel}} \times P\left(\frac{\lambda}{\lambda_{R0}}\right)\left(\frac{t}{10 \text{ days}}\right)^{0.5} \text{mJy} . \tag{21}$$

The observed spectral evolution can for $t \lesssim 100$ days be fitted by

$$F_\nu = 1.6 \times 10^2 P\left(\frac{\lambda}{\lambda_{R0}}\right)\left(\frac{t}{10 \text{ days}}\right)^{0.62} \text{mJy} . \tag{22}$$

Therefore,

$$N_{\text{rel}} = 1.4 \times 10^{25} \dot{M}^{-2.25}\left(\frac{V}{2 \times 10^4 \text{ km s}^{-1}}\right)^{2.5} \times \left(\frac{t}{10 \text{ days}}\right)^{0.11} \text{cm}^{-2} \tag{23}$$

for $t \lesssim 100$ days.

As a consistency check of the assumption of $\tau_s \ll 1$, from equation (8) we can now calculate the synchrotron self-absorption optical depth with the above values of B and N_{rel}. One then finds that, because of the Razin suppression of the opacity, the optical depth at λ_{R0} does not exceed 0.1 at any time.

A fatal problem for the Razin model occurs when we estimate the energy density of relativistic electrons, u_{rel}. We will be conservative here and just include electrons with Lorentz factors responsible for the observed spectrum between 10 and 100 days, i.e., wavelengths of 1.3–6.3 cm, giving $1.1 \times 10^2 (t/10 \text{ days})^{0.57} \lesssim \gamma \lesssim 2.4 \times 10^2 (t/10 \text{ days})^{0.57}$. From equation (23) and $p = 3.5$ we find that the energy per unit area within this band is $\sim 4.7 \times 10^{15} (t/10 \text{ days})^{-0.75}$ ergs cm^{-2}, which is only weakly dependent on p. As we show in § 3.2.1 [eq. [37] with $L_{\text{bol}} \approx 4 \times 10^{42} (t/10 \text{ days})^{-0.9}$ ergs s^{-1}], inverse Compton losses are in this case likely to be important down to $\gamma \approx 30$. This implies in the Razin case that the inverse Compton timescale during the first 100 days is $t_{\text{Comp}} \sim 0.36 (t/10 \text{ days})^{2.4} \lambda^{0.5}$ days. The thickness of the emitting region is $\Delta R_{\text{em}} \approx V t_{\text{Comp}}/4$, or for $\lambda \sim 3$ cm $\Delta R_{\text{em}} \approx 2.5 \times 10^{13} (t/10 \text{ days})^{2.4}$ cm. The energy density is then $u_{\text{rel}} \approx 1.9 \times 10^2 (t/10 \text{ days})^{-3.1}$ ergs cm^{-3}. This can be compared with the

thermal energy density behind the shock, $u_{\rm thermal} \approx 3.4 \times 10^2 \dot{M}(t/10 \text{ days})^{-2}$ ergs cm^{-3}, which is only slightly higher than $u_{\rm rel}$.

Our estimate of $u_{\rm rel}$ is most likely a serious underestimate, since we have only included the spectrum between wavelengths 1.3 and 6.3 cm [already at 21 cm, $\gamma \sim 60(t/10 \text{ days})^{0.57}$]. In reality, one should extrapolate the electron spectrum down to $\gamma \sim 1$, which could increase the energy density by a factor of $\gamma(\lambda = 1.3 \text{ cm})^{1.5} \gtrsim 300$. The exact factor depends on the detailed cooling processes as well as the form of the spectrum close to $\gamma \sim 1$ and is therefore model dependent. However, this will not alter our main conclusion that *the energy density of relativistic electrons in this model is likely to exceed the energy density of thermal particles by a large factor*, which is unrealistic in any model for the particle acceleration and rules out this model. Typical values of the injection efficiency are instead $\lesssim 10^{-2}$ (e.g., Chevalier 1982b). The main reason for this problem is the weak magnetic field and the steep power-law index derived from the Razin cutoff. Because $F_\nu \propto N_{\rm rel} B^{\alpha+1}$, this results in a very large value of $N_{\rm rel}$.

3.1.2. *Synchrotron Self-Absorption Plus Free-Free External Absorption*

The fact that the Razin model requires an unrealistically large density of nonthermal electrons, because of the low magnetic field, forces us to more complex models. The most natural one is then a combination of synchrotron self-absorption and external free-free absorption. The latter component has the effect of suppressing the too high flux at long wavelengths in the synchrotron self-absorption model. As we will find, this model also solves the efficiency problem above by requiring a higher magnetic field, while at the same time giving a free-free absorption consistent with earlier estimates in FLC96.

To model the combined absorption, we now use equation (1), integrated over the supernova disk, but still assuming a fixed spectral index. We then have $\tau_s(1 \text{ cm})$ and $\tau_{\rm ff}(1 \text{ cm})$ as free parameters, in addition to α and S'.

For a given temperature, $T_e(r)$, and including the Gaunt factor, $g_{\rm ff}$, the free-free optical depth along a ray with impact parameter s is given by

$$\tau_{\rm ff}(t, s) = 5.63 \times 10^{53} \dot{M}^2 \lambda^2 \frac{(1+2X)}{(1+4X)} \times \int_{R_s}^{\infty} \frac{\{-2.78 + \log [\lambda T_e^{3/2}(r)]\}}{T_e(r)^{3/2} r^3 (r^2 - s^2 R_s^2)^{1/2}} \, dr \, , \quad (24)$$

where $X = X(\text{He})/X(\text{H})$. $\tau_{\rm ff}$ is therefore sensitive to the radial temperature profile, as well as its dependence on time. Lundqvist & Fransson (1988), as well as FLC96, have discussed the determination of this extensively, and it is found that at radii $\lesssim 1 \times 10^{16}$ cm the gas cools rapidly from $\gtrsim 1 \times 10^6$ K to $\sim 2.5 \times 10^5$ K, while at large radii the temperature is fairly constant at $\sim$(2–2.5) $\times 10^5$ K. Therefore, as the shock propagates outward, the gas close to the shock will initially have a decreasing temperature, while later it will be more constant. This is seen clearly for SN 1993J in Figure 11 of FLC96. While this behavior is probably quite generic, the details of the radial variation depend strongly on the properties of the shock radiation (see § 4.1).

In this paper we use a simple parameterization of the temperature profile, assumed to be constant with time, and given by

$$T_e(r) = \max \left[T_{15} \left(\frac{10^{15} \text{ cm}}{r} \right)^{\delta}, 2 \times 10^5 \text{ K} \right]. \quad (25)$$

We then vary the parameters T_{15} and δ to get an optimum fit of the spectra. Although indicative of the actual temperature, equation (25) should only be interpreted as a convenient fitting formula. The reason is that the fundamental parameter for the fitting of the spectra is not $T_e(r)$, but rather $\tau_{\rm ff}(t)$. As shown by equation (24), the same $\tau_{\rm ff}(t)$ can be obtained by different $\dot{M}$ and $T_e(r)$, as long as $\dot{M}^2 \times \int T_e(r)^{-3/2} r^{-4} \, dr \approx$ constant. Different temperature profiles can therefore yield the same result for $\tau_{\rm ff}(t)$. The value of T_e given by equation (25) should therefore only be interpreted as a weighted average. Also, the dependence of T_e on $\dot{M}$ should be kept in mind when interpreting the results.

We have calculated the best fit for different values of α, T_{15}, and δ, when $S'(t)$ and $\tau_s(t)$ are varied for each date. We find that good fits are obtained for $\delta = 1.0$ and $T_{15} = 2.75 \times 10^6$ K, with $\chi_\nu^2 = 1.4$–1.5. Larger and smaller values of δ give considerably higher χ_ν^2. The free-free absorption is well determined only by the spectra and light curves later than $\sim$10 days. We have tested different values of the spectral index and find that we get a best fit with $\alpha = 0.85$, or $p = 2.7$. Because the quality of the fit is very similar to that in the more detailed model in Figure 8, we do not show it here.

In Figure 4 we show the evolution of the wavelength at which the synchrotron self-absorption optical depth is

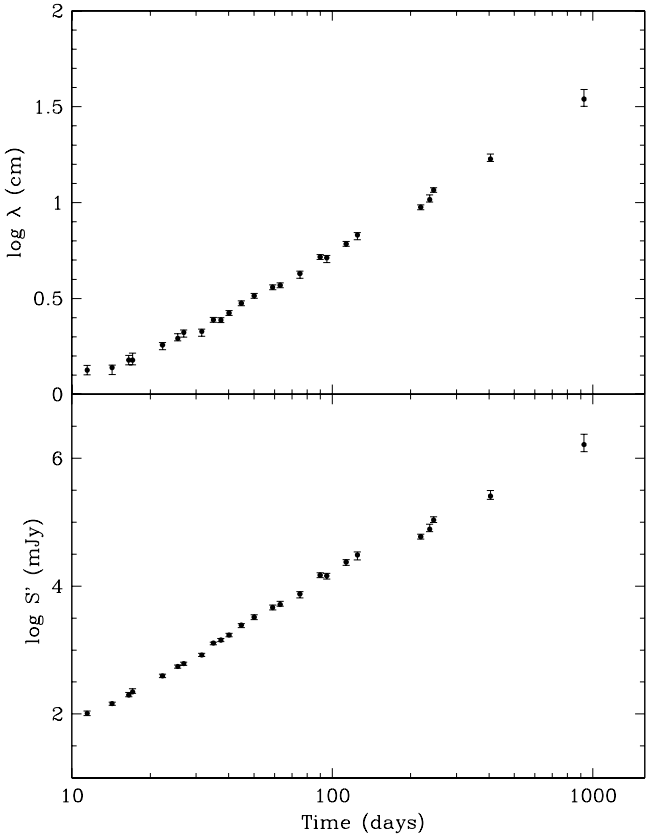

FIG. 4.—Evolution of $\lambda_{\tau_{\rm ssa}=1}$ and the scaled source function $S'(t) = \pi S(t) R(t)_s^2 / D^2$ for the synchrotron self-absorption model with external free-free absorption.

unity, $\lambda_{\tau_{ssa}=1} = \tau_s(t)^{-1/(5/2+\alpha)}$, and the scaled source function at 1 cm, $S'(t)$. A least-squares fit to the observations for $10 < t < 100$ days gives

$$\lambda_{\tau_{ssa}=1} = \lambda_{10}\left(\frac{t}{10 \text{ days}}\right)^{q_\lambda}, \quad (26)$$

with $\lambda_{10} = 1.07$ cm and $q_\lambda = 0.68$. For $t \gtrsim 100$ days the evolution gets steeper and $\lambda_{10} = 0.81$ cm and $q_\lambda = 0.81$. The dispersion in the exponent is ± 0.03. Similarly, the variation in S' can for 10–100 days be fitted by

$$S'(t) = S_{10}\left(\frac{t}{10 \text{ days}}\right)^{q_S}, \quad (27)$$

where $S_{10} = 60.1$ mJy and $q_S = 2.43$, while at later times ($\gtrsim 100$ days) the evolution is less steep with $S_{10} = 1.67 \times 10^2$ mJy and $q_S = 2.00$.

Knowing $\lambda_{\tau_{ssa}=1}(t)$ and $S'(t)$, we can now calculate the magnetic field and the column density of relativistic particles:

$$B(t) = 9.45 \times 10^{-8} c(p)^2 \left(\frac{R_s}{D}\right)^4 S'(t)^{-2}, \quad (28)$$

where

$$c(p) = \frac{(p + 7/3)}{(p + 10/3)(p + 1)} \times \frac{\Gamma[(p + 8)/4]\Gamma[(p + 5)/4]\Gamma[(3p - 1)/12]\Gamma[(3p + 7)/12]}{\Gamma[(p + 6)/4]\Gamma[(p + 7)/4]\Gamma[(3p + 2)/12]\Gamma[(3p + 10)/12]} \quad (29)$$

and Γ is the gamma function. The column density of relativistic particles is then given by

$$N_{rel}(t) = \frac{1.98 \times 10^{17}}{(1.18 \times 10^{-2})^p} \times \frac{\Gamma[(p + 8)/4]}{(p + 10/3)\Gamma[(p + 6)/4]\Gamma[(3p + 2)/12]\Gamma[(3p + 10)/12]} \times B^{-(p+2)/2} \lambda_{\tau_{ssa}=1}^{-(p+4)/2} \text{ cm}^{-2}. \quad (30)$$

As is seen from equations (28) and (30), both $B(t)$ and $N_{rel}(t)$ depend on $R_s(t)$, which in turn is determined by the ejecta structure. In this section we assume for simplicity a constant velocity of $V = 2.2 \times 10^4$ km s^{-1} (see § 3.2.3).

The resulting magnetic field and column density are given in Figure 5. During most of the observed interval the decrease in B is approximately a power law, and such a fit gives

$$B(t) = 25.5\left(\frac{t}{10 \text{ days}}\right)^{-0.93 \pm 0.08}\left(\frac{V}{2.2 \times 10^4 \text{ km s}^{-1}}\right)^4 \text{ G}. \quad (31)$$

Within the errors, $N_{rel}(t)$ is nearly constant, although the scatter increases considerably for $t \gtrsim 100$ days. The level of N_{rel} in Figure 5 should be compared with that in the Razin model from § 3.1.1. Because of the higher magnetic field, and most importantly the smaller value of p, N_{rel} is roughly 6 orders of magnitude smaller than for the Razin model.

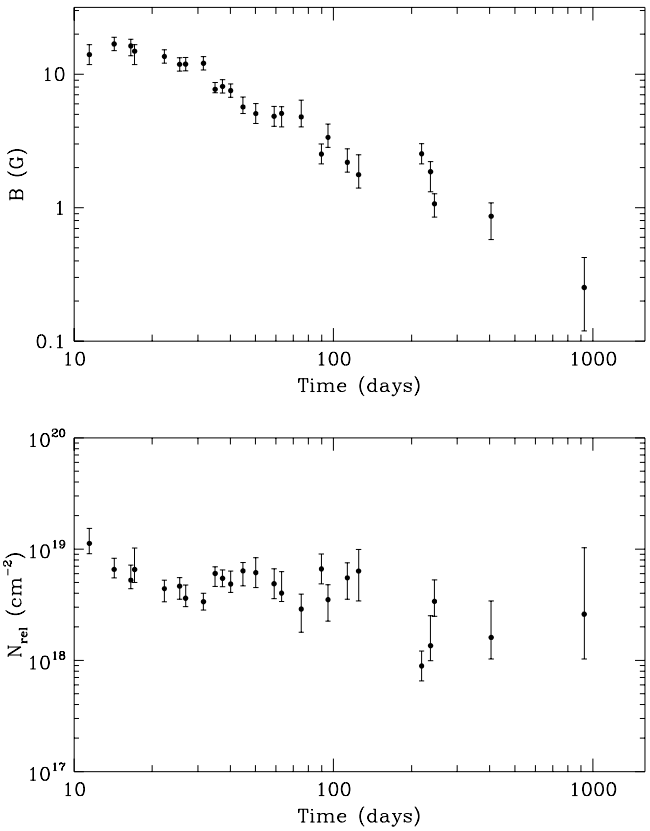

FIG. 5.—Evolution of the magnetic field and column density of relativistic electrons in the synchrotron self-absorption plus external free-free absorption model.

With the magnetic field in equation (31) we can calculate the Razin wavelength from equation (18)

$$\lambda_{R0} = 3.5 \times 10^2 \dot{M}\left(\frac{V}{2.2 \times 10^4 \text{ km s}^{-1}}\right)^2\left(\frac{t}{10 \text{ days}}\right) \text{ cm}. \quad (32)$$

Comparing equations (26) and (32) we find that the Razin effect in this model is unimportant.

Although the above results are of great interest, and will be discussed in detail below, there are several deficiencies in the analysis. The most serious limitation is that we have assumed a constant power-law electron spectrum, i.e., neglected possible losses by radiation or collisions. Therefore, we will now, at the expense of a more complicated model, discuss a self-consistent analysis of the observations. The discussion in this section, however, is of great help in order to understand the different processes involved, as well as being a guide to the values of B and N_{rel} and their sensitivity to different parameters.

3.2. *Self-consistent Analysis*

3.2.1. *Energy Losses of the Nonthermal Electrons*

For formulating a self-consistent analysis, it is necessary to discuss possible energy losses of the electrons that will affect the integrated electron spectrum, and therefore also the emission from the plasma. To estimate these effects, we assume in this subsection that the magnetic field behaves

like

$$B(R_s) = B_{10}\left(\frac{t}{10\ \mathrm{days}}\right)^{-1}, \tag{33}$$

where B_{10} parameterizes the strength of the field. From our earlier discussion and anticipating the results below, we expect $B_{10} \approx 30$ G, to which we scale our estimates. To express our results as a function of time rather than radius, we use in this section $R(t) = 1.72 \times 10^{15}(t/10\ \mathrm{days})$ cm, corresponding to a constant velocity of $V = 2 \times 10^4$ km s^{-1}.

We first estimate the typical Lorentz factor for the relativistic electrons responsible for the radiation at wavelength λ from $\gamma \approx 85(\lambda B)^{-1/2}$, or

$$\gamma = 15.5\left(\frac{t}{10\ \mathrm{days}}\right)^{1/2}\left(\frac{B_{10}}{30\ \mathrm{G}}\right)^{-1/2}\lambda^{-1/2}. \tag{34}$$

The synchrotron lifetime for an electron to decrease its energy by a factor of 2 is

$$\frac{t_{\mathrm{synch}}}{t} = 1.0\gamma^{-1}\left(\frac{B_{10}}{30\ \mathrm{G}}\right)^{-2}\left(\frac{t}{10\ \mathrm{days}}\right). \tag{35}$$

In terms of the observed wavelength, this becomes

$$\frac{t_{\mathrm{synch}}}{t} = 6.4 \times 10^{-2}\,\lambda^{1/2}\left(\frac{B_{10}}{30\ \mathrm{G}}\right)^{-3/2}\left(\frac{t}{10\ \mathrm{days}}\right)^{1/2}. \tag{36}$$

It is obvious that synchrotron losses are important throughout most of the observed period.

Because of the strong background radiation field from the supernova, inverse Compton losses may be important for the relativistic electrons. One can estimate the timescale for this from

$$\frac{t_{\mathrm{Comp}}}{t} = \frac{3}{16\pi}\frac{m_e c^2}{\gamma\sigma_{\mathrm{T}} J_{\mathrm{Bol}}} \approx 40\gamma^{-1}\left(\frac{L_{\mathrm{Bol}}}{10^{42}\ \mathrm{ergs\ s^{-1}}}\right)^{-1} \times \left(\frac{V}{2 \times 10^4\ \mathrm{km\ s^{-1}}}\right)^2\left(\frac{t}{10\ \mathrm{days}}\right), \tag{37}$$

where J_{Bol} and L_{Bol} are the bolometric mean intensity and luminosity, respectively.

The bolometric luminosity has contributions from both the ejecta, powered by the thermal energy from the passage of the shock and later by radioactive decay, and radiation produced by the circumstellar interaction. The ejecta flux is emitted mainly in the optical and at early time also in the UV. We estimate the ejecta luminosity from the bolometric luminosity calculated by Young, Baron, & Branch (1995), from observations by Richmond et al. (1994) and Lewis et al. (1994). Unfortunately, the reddening is uncertain. A range in E_{B-V} of 0.08–0.32 has been estimated by Richmond et al. Unless otherwise stated, we will use $E_{B-V} = 0.08$ in the following.

The luminosity in X-rays from the circumstellar and reverse shocks are calculated in FLC96 and Fransson (1998). The circumstellar shock is important only for $t \lesssim 10$ days, and based on Figure 8 in FLC96, scaled to $\dot{M} = 1$, we estimate $L_{\mathrm{cs}} = 3.1 \times 10^{41}(t/10\ \mathrm{days})^{-1.2}$ ergs s^{-1}. To include both the in-going and outgoing radiation we multiply the results in FLC96 by a factor of 2. In Fransson (1998) the evolution of the reverse shock luminosity is calculated for realistic density profiles, and it is found that $L_{\mathrm{rev}} = (1\text{–}2) \times 10^{41}$ ergs s^{-1}.

The mean intensity, J_i, of the different luminosity components at the position of the circumstellar shock is given by $J_i = WL_i/4\pi^2R_i^2$, where $W = \frac{1}{2}\{1 - [1 - (R_i/R_s)^2]^{1/2}\}$ is the dilution factor. The radius R_i stands for either the photospheric radius, R_{ph}, or the shock radius in the two cases. For $R_{\mathrm{ph}} \ll R_s$, $J \approx L_{\mathrm{ej}}/16\pi^2R_s^2$. The radiation from the shocks is more isotropic at the circumstellar shock. Depending on the thickness of the circumstellar shock and the location of the acceleration zone, one expects that $R_s \approx (1.0\text{–}1.3)R_{\mathrm{rev}}$.

In Figure 6 we show the resulting total mean intensity multiplied by $16\pi^2R_s^2$, together with the individual contributions from the ejecta and the shock waves for $\dot{M} = 1$. In the case that $R_i \ll R_s$, this essentially gives the total luminosity from component i. During the first $\sim$100 days, the radiation density is dominated by the ejecta, with an increasing contribution from the reverse shock, and can be approximated by $L_{\mathrm{bol}} \approx 4 \times 10^{42}(t/10\ \mathrm{days})^{-0.9}$ ergs s^{-1}.

The Compton scattered optical photons from the ejecta and the thermalized X-rays from the reverse shock emerge at $h\nu \approx \gamma^2 h\nu_0 \approx 0.1$–100 keV. For our parameters, the luminosity in this range is $\sim 2.5 \times 10^{35}(L_{\mathrm{synch}}/10^{37}$ ergs s^{-1}$)(L_{\mathrm{bol}}/10^{42}$ ergs s^{-1}$)$ ergs s^{-1}. The free-free flux from the shock (FLC96) therefore dominates the X-rays. One can also show that the ratio between first- and second-order Compton scatterings (Rees 1967) is small.

Knowing both the magnetic field and the radiation density, we can calculate the critical value of the Lorentz factors, γ_{synch} and γ_{Comp}, for which the synchrotron and Compton timescales are equal to the expansion timescale. In Figure 7 this is shown as the solid line. We also show the approximate value of γ for the electrons responsible for the emission at 1 and 21 cm, $\gamma_{1\ \mathrm{cm}}$ and $\gamma_{21\ \mathrm{cm}}$, respectively, as given by equation (34). Clearly, synchrotron losses are more important than inverse Compton losses at all times.

Coulomb losses can also be important for the relativistic electrons. For these electrons the ratio of the Coulomb timescale to the expansion timescale is given by

$$\frac{t_{\mathrm{Coul}}}{t} = 8.9 \times 10^{-3}\gamma\dot{M}^{-1}\left(\frac{V}{2 \times 10^4\ \mathrm{km\ s^{-1}}}\right)^2\left(\frac{t}{10\ \mathrm{days}}\right). \tag{38}$$

For $\gamma \lesssim \gamma_{\mathrm{Coul}} = 1.1 \times 10^2(t/10\ \mathrm{days})^{-1}$ Coulomb losses are important. We should also compare t_{Coul} with the synchrotron timescale, and we find that for

$$\gamma \lesssim \gamma_{\mathrm{s\text{-}C}} = 8.62\dot{M}^{1/2}\left(\frac{B_{10}}{30\ \mathrm{G}}\right)^{-1}\left(\frac{V}{2 \times 10^4\ \mathrm{km\ s^{-1}}}\right)^{-1} \tag{39}$$

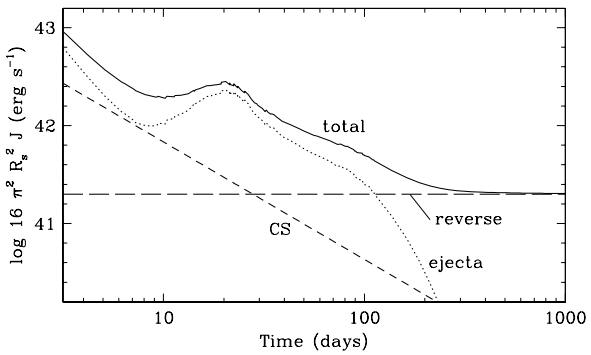

FIG. 6.—Evolution of the mean intensity, J, at the shock, for $E_{B-V} = 0.08$, $\dot{M} = 5 \times 10^{-5}\,M_\odot$ yr^{-1}, and $u_w = 10$ km s^{-1}. The quantity $16\pi^2R_s^2J$ is essentially the total luminosity at the shock.

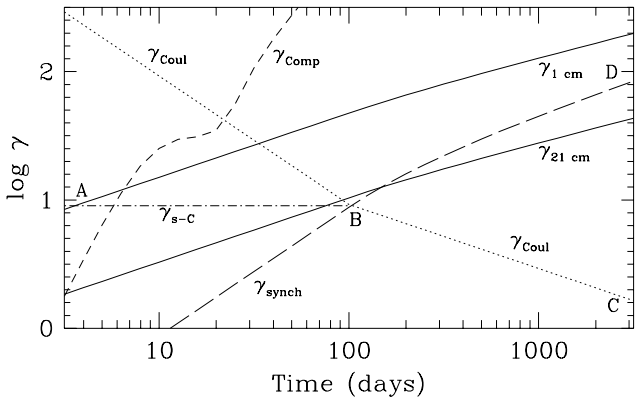

FIG. 7.—Lorentz factor, γ_{synch}, γ_{Comp}, γ_{Coul}, for which the synchrotron, inverse Compton, and Coulomb loss times, respectively, are equal to the expansion time. The dot-dashed line shows the region below which Coulomb losses are more important than synchrotron losses. Below the line ABC Coulomb losses dominate, and above the line ABD synchrotron losses dominate, while the region CBD is adiabatic. The typical γ responsible for the emission at 1 and 21 cm are shown as solid lines.

Coulomb losses dominate synchrotron losses. In Figure 7 we show γ_{Coul} and $\gamma_{s\text{-}C}$ for $\dot{M} = 1$. We note that $\gamma_{s\text{-}C}$ is independent of time and that especially at early times Coulomb cooling is important for the longer wavelengths.

Synchrotron and inverse Compton losses steepen the electron spectrum index by one (e.g., Pacholczyk 1970, and § 5 below). Coulomb losses have the opposite effect to synchrotron losses in that the electron spectrum index flattens by one power, compared with the injected spectrum. Therefore, with the parameters in Figure 7, we expect that before ~ 100 days (i.e., when $\gamma_{synch} \sim \gamma_{Coul}$) the electron spectrum will be flattened by one power for energies below $\gamma_{s\text{-}C}$ and steepened by one power above $\gamma_{s\text{-}C}$. In reality, both Coulomb and synchrotron compete in the regions responsible for the observed emission, and the spectral index is intermediate between these values. Later than ~ 100 days, the electron spectrum will have three regions, one between $\gamma_{Coul} < \gamma < \gamma_{synch}$, where the spectrum is equal to the original input spectrum, while below and above this region the spectrum is flattened and steepened by one power in energy, respectively. We return to this issue in § 5.

3.2.2. *Calculation of the Electron Spectrum*

For the acceleration of the relativistic electrons, once they have been injected from the thermal pool, there are at least two possibilities. First-order Fermi acceleration across the circumstellar shock is an obvious candidate, but acceleration in the turbulent region close to the contact discontinuity is also a possibility (Chevalier, Blondin, & Emmering 1992). The timescale of acceleration depends on the spatial diffusion coefficient, and therefore on the mean free paths. Only rough estimates of the timescale based on modeling of the radio emission from SN 1987A are available (Ball & Kirk 1992; Duffy, Ball, & Kirk 1995). From the expression given by Ball & Kirk (1992) for the variation of flux with time (their eq. [8]) we find that the rise is likely to be very rapid, $t_{acc} \ll 10$ days. Here, we therefore assume that the electrons are accelerated almost instantaneously (i.e., $t_{acc} \ll t_{Comp}, t$), with a spectrum $\propto \gamma^{-p_i}$.

In calculating the electron distribution we use the equation

$$\frac{\partial N(\gamma)}{\partial t} = \frac{\partial}{\partial \gamma}\left[\frac{\gamma}{t_{loss}} N(\gamma)\right] + \frac{\partial}{\partial \gamma}\left\{E(\gamma)\gamma^2 \frac{\partial}{\partial \gamma}\left[\frac{N(\gamma)}{\gamma^2}\right]\right\} - \frac{N(\gamma)}{t_{esc}} + \frac{(p_i - 1)Vn_{rel}}{4\gamma_{min}}\left(\frac{\gamma_{min}}{\gamma}\right)^{p_i}. \quad (40)$$

The first term on the right-hand side takes all energy losses into account, with a total energy loss timescale given by

$$t_{loss} = \left(\frac{1}{t_{synch}} + \frac{1}{t_{Comp}} + \frac{1}{t_{Coul}} + \frac{1}{t}\right)^{-1}. \quad (41)$$

The first three terms on the right-hand side of equation (41) are already defined, while the last term takes adiabatic losses into account. In equation (40) the second term, where $E(\gamma)$ is given by

$$E(\gamma) = \frac{1}{2m_e^2 c^2}\int j(\nu, \gamma)\frac{J_\nu}{\nu^2}\, d\nu\,, \quad (42)$$

accounts for the heating of the nonthermal electrons by the radiation. In this, $j(\nu, \gamma)$ is the single electron emissivity. The third term of equation (40) describes the escape of particles, either as a result of advection toward the contact discontinuity, and subsequent energy degradation by collisions in the high-density gas, or as a result of actual escape. Finally, the last term gives the number of injected electrons with energy $\gamma m_e c^2$ per second and unit area, which we assume to be instantaneously accelerated at the shock. A similar equation was first used by McCray (1969) to discuss the thermalization of the electron distribution, when synchrotron self-absorption is important, while the form given here is basically that used by de Kool, Begelman, & Sikora (1989). The equation assumes that the electrons are relativistic, but given our ignorance of the details of the injection process, which certainly influences the distribution for $\gamma \sim 1$, this is sufficient. Equation (40) is solved by the semi-implicit method of Chang & Cooper (1970).

If we assume that the self-absorption effects are small and that the escape term can be ignored to a reasonable approximation, as is confirmed by the detailed calculations in § 5, we can write down the stationary solution to equation (40) as

$$N(\gamma) = \frac{n_{rel} Vt}{4\gamma_{min}}\left(\frac{\gamma}{\gamma_{min}}\right)^{-p_i}\left(1 + \frac{t}{t_{Coul}} + \frac{t}{t_{Comp}} + \frac{t}{t_{synch}}\right)^{-1}. \quad (43)$$

With this electron spectrum we can calculate the synchrotron emissivity and opacity from the general expressions in equations (6) and (8), as well as the source function, and finally the synchrotron spectrum as function of time.

Because $V(t)$, L_{bol}, and $\dot{M}$ are determined from other observations (§ 3.2.3), we have for each spectrum two parameters, n_{rel} and B. We have to further assume a specific *input* spectrum for the electrons (i.e., p_i), which we take to be constant with time.

3.2.3. *Velocity Evolution*

The magnetic field and electron density depend on the velocity evolution of the shock, i.e., on R_s (e.g., eq. [28]). The velocity of the shock region is in turn sensitive to the density structure of the ejecta. If the ejecta density is approximated by a power law with an exponent n, the shock radius varies

as $R_s \propto t^m$, where, for an $n_e \propto r^{-2}$ wind, $m = (n-3)/(n-2)$ (Chevalier 1982a). A flat density profile, $n \lesssim 7$, causes the shock to slow down, while a steep profile, $n \gtrsim 20$, gives a shock of fairly constant velocity. Unfortunately, the density structure of the ejecta is uncertain, depending on an equally uncertain progenitor structure. Optical line profile observations of SN 1993J provide some constraint on $V(t)$. This, however, refers to the ejecta gas and not directly to the radio emitting plasma, which is likely to be 20%–30% farther out. Also, if there is a change in the density gradient, one can expect a lag of the adjustment to the new gradient.

The most direct information about the size of the radio emitting region comes from VLBI observations. During the first 92 days Bartel et al. (1994) found roughly undecelerated expansion, $m = 0.96 \pm 0.07$, with a velocity $V = 19{,}000 \pm 3000$ km s^{-1}. Most of the uncertainty in V comes from the M81 distance errors, $D = 3.63 \pm 0.34$ Mpc (Freedman et al. 1994), which do, however, not enter in m. At later times, 182–1304 days, Marcaide et al. (1997) find strong evidence for deceleration, with $m \approx 0.86 \pm 0.02$. It is quite possible that the VLBI velocities above are underestimated. FLC96, as well as Bartel et al., argue that the Hα line indicated an ejecta velocity of 18,000–19,000 km s^{-1} at 10–30 days. The shock velocity should be a factor of 1.2–1.3 larger than this, or 21,600–24,700 km s^{-1}. Furthermore, the VLBI measurements have a fairly small dynamic range;

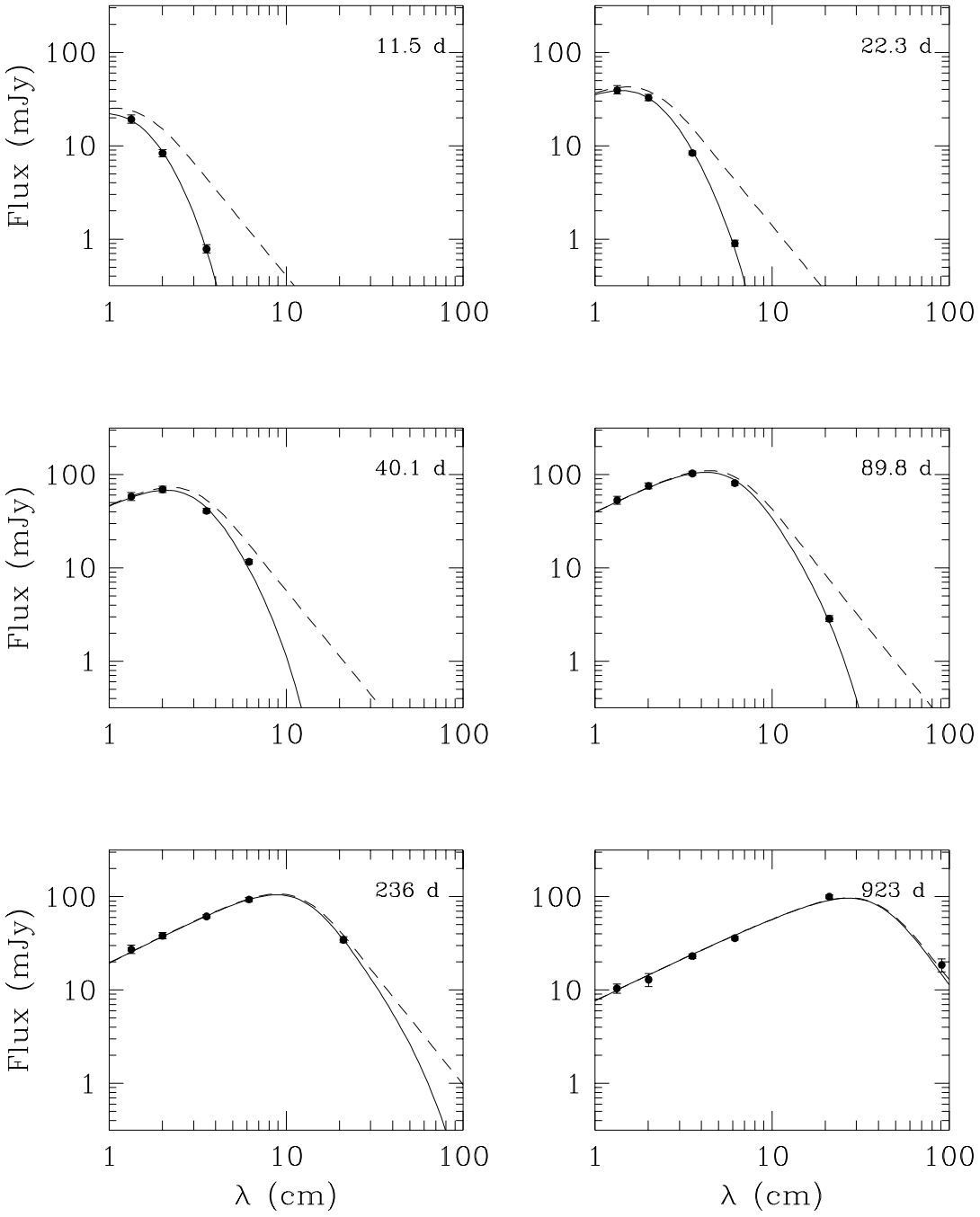

FIG. 8.—Fits to the VLA spectra at six different epochs, including all suppression processes, as well as a self-consistent calculation of the electron spectrum. The dashed line shows the intrinsic spectrum from the shock, while the solid line also includes external free-free absorption.

faint, high-velocity material may therefore go undetected. We also point out that the radius measured by Marcaide et al. only refers to the 50% contour level, which explicitly excludes such faint, high-velocity material. Guided by this discussion we will in the following parameterize the velocity by

$$V(t) = \begin{cases} V_0 & t < t_p \, , \\ V_0 \left(\dfrac{t}{t_p} \right)^{(m-1)} & t_p \leq t \, , \end{cases}$$

with $V_0 = 22{,}000$ km s^{-1}. Because we take $V =$ constant for $t < t_p$, our value of m will be less than the value of $m = 0.86$ from Marcaide et al. With $t_p = 100$ days our effective value of m up to day 1304 is $m = 0.74$, corresponding to $n \approx 6$. Using $t_p = 200$ days would not change our results significantly.

4. RESULTS

With all parameters fixed, except B, $n_{\rm rel}$, and p_i, we can now repeat the modeling in § 3.1.2 for each date, thereby determining the unknown parameters from a χ^2 fit. However, in contrast to § 3.1.2, we take the different cooling processes into account. The resulting spectra at six epochs, from 11.5 to 923 days, are shown in Figure 8. Also shown is the spectrum when free-free absorption is neglected. It is seen that when the latter process is included the fit is essentially perfect, as is the case also for the other dates. We now discuss the implications for the physical parameters resulting from this procedure.

4.1. *Free-Free Absorption*

The analysis in § 3.1.2 shows that the best fits for the free-free absorption are obtained for $\delta = 1.0$ and $T_{15} = 2.75 \times 10^6$ K and an asymptotic temperature of 2×10^5 K.

This, and the evolution of temperature derived from the observations, can be compared with the calculations in FLC96. At 10 days FLC96 (their Fig. 11) find that at a radius of $1.5 \times R_s$, $T_e \approx 6.3 \times 10^5$ K, decreasing to 3.0×10^5 K at 20 days and then staying at a constant value of 2.5×10^5 K up to day 100.

As we stressed in § 3.1.2, the most relevant quantity to compare with the observations is not the temperature, but the optical depth. A further complication is that the temperature in FLC96 not only varies with radius, but, contrary to our model assumptions, it also shows some variation with time at a given radius. For a real comparison one should perform the radial integration of the optical depth at each time [i.e., $\tau_{\rm ff} \propto \int_{R_s}^{\infty} T_e(r,\ t)^{-1.5} n_e(r)^2 dr$]. In Figure 9 we show the free-free optical depth, averaged over the disk, for the $\rho \propto r^{-2}$ model in FLC96 along with that determined by the observations. In general the two results agree to better than a factor of 2. While the difference is significant, we feel that it is remarkable that they agree as well as they do, and that this agreement gives us increased confidence in the determination of the circumstellar temperature from the model calculations not only in the case of SN 1993J, but also for other objects like SN 1979C and SN 1980K (Lundqvist & Fransson 1988). An approximate fit to our results in Figure 9 is given by

$$\bar{\tau}_{\rm ff}(t) = 0.12 \lambda^{2.1} \left(\frac{t}{10 \text{ days}} \right)^{-2.1} . \qquad (44)$$

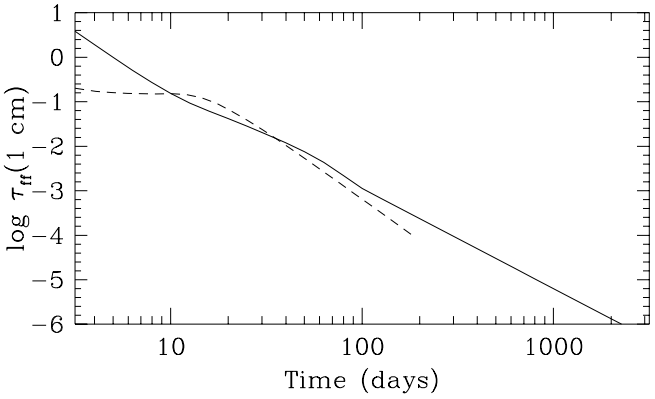

FIG. 9.—The free-free optical depth at 1 cm determined from the fits in this paper, compared with the optical depth from the model calculations of the circumstellar temperature in FLC96 (*dashed line*).

The fact that we get a power law significantly flatter than t^{-3} even in the constant temperature region at $t \gtrsim 100$ days is due to the compensating effect of the decreasing velocity, which gives an approximate power-law dependence over the whole period.

Although in broad agreement with the optical depth required by our modeling, there are considerable uncertainties in the calculation of the temperature of the circumstellar medium, as is discussed in FLC96. Most important of these are the degree of equipartition of electrons and ions behind the circumstellar shock, and the evolution of the shock velocity shortly after breakout. Both affect the temperature of the shocked electrons, as well as the electron scattering optical depth. These two quantities determine the UV and soft X-ray flux from the shock through Comptonization of the soft photospheric photons. The uncertainty in the shocked electron temperature is therefore reflected in the absolute value and the radial dependence of the temperature of the circumstellar medium. The radio observations therefore provide a new constraint on the physics and radiation mechanisms of the shock.

4.2. *Magnetic Field*

In Figure 10 we show the resulting magnetic field as a function of the shock radius. The errors in B and $n_{\rm rel}$ are determined from the 1 σ contours of constant χ^2 in the

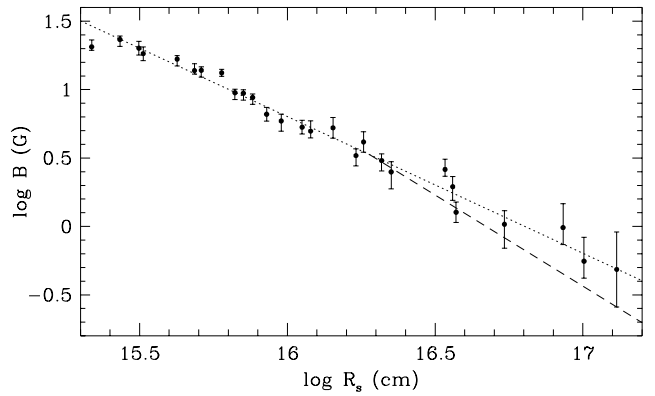

FIG. 10.—Evolution of the magnetic field as a function of shock radius. The dashed line shows the expected evolution if $B^2 \propto \rho_{\rm wind} V_s^2$, while the dotted line shows the evolution of a $B \propto R_s^{-1}$ field.

B-$n_{\rm rel}$ plane. The scatter in $B(t)$ at late times is related to the scatter in $S'(t)$, which enters quadratically in $B(t)$.

A least-squares fit to the data shows that

$$B(t) = B_{15}\left(\frac{R_s}{10^{15}\ \mathrm{cm}}\right)^{-\beta}\left(\frac{V_0}{2.2\times 10^4\ \mathrm{km\ s^{-1}}}\right)^4, \quad (45)$$

with $B_{15} = 61.1 \pm 4.7$ G and $\beta = 0.984 \pm 0.028$. As seen by the dotted line in Figure 10, it is certainly compatible with a simple $B \propto R_s^{-1}$ law. A best fit with this dependence is given by $B_{15} = 63.5 \pm 4.8$ G ($\beta \equiv 1.0$). Note that the errors do not include systematic errors. In particular, the results are, as shown by the expressions above, sensitive to the velocity evolution, as well as its absolute value.

A $B \propto R_s^{-1}$ dependence is close to that expected if the magnetic field behind the shock is amplified by a constant factor from the circumstellar magnetic field of a rotating progenitor. If the wind has sufficient angular momentum, the magnetic field should have the topology of a "Parker spiral" at large radii (Parker 1958; Weber & Davis 1967). In this case one expects $B \propto r^{-1}$, while a radially expanding wind has $B \propto r^{-2}$.

The magnetic fields of the circumstellar media of late type supergiants are uncertain. Based on polarization observations of OH masers in supergiants, Cohen et al. (1987) and Nedoluha & Bowers (1992) estimate that at a radius of $\sim 10^{16}$ cm the magnetic field is $\sim$1–2 mG, although the uncertainty in this number is large. It is unlikely that the magnetic field in the wind is higher than that corresponding to equipartition between the magnetic field and the kinetic energy of the wind. This means that $B^2/8\pi \lesssim \rho u_{\rm w}^2/2$, giving

$$B \lesssim \frac{(\dot{M}u_{\rm w})^{1/2}}{r} = 2.5\left(\frac{\dot{M}}{10^{-5}\ M_\odot\ \mathrm{yr^{-1}}}\right)^{1/2} \times \left(\frac{u_{\rm w}}{10\ \mathrm{km\ s^{-1}}}\right)^{1/2}\left(\frac{r}{10^{16}\ \mathrm{cm}}\right)^{-1}\ \mathrm{mG}\,. \quad (46)$$

Likely locations for the electron acceleration are at the position of the circumstellar shock or, alternatively, close to the contact discontinuity between the circumstellar swept-up gas and the shocked ejecta gas. The latter region is Rayleigh-Taylor unstable, and the associated turbulence may help in amplifying the magnetic field (Chevalier et al. 1992; Jun & Norman 1996).

At 10 days, corresponding to a radius $\sim 1.9 \times 10^{15}$ cm, we find that the magnetic field in the emitting region is $\sim$34 G. Using the above estimate of the circumstellar magnetic field and a shock compression by a factor of 4, this post-shock magnetic field would be $B \approx (2.4\text{–}4.8) \times 10^{-2}$ G. This is a factor $\sim 10^3$ less than that inferred from the observations and therefore strongly argues for magnetic field amplification behind the shock. Although this conclusion rests on the very uncertain estimate of the circumstellar magnetic fields of the progenitor system, a simple shock compression of the field can probably be excluded and gives support to the results found in the simulations by Jun & Norman (1996).

If the scaling of the magnetic field is based on the thermal energy density, one expects $B^2/8\pi \propto \rho V^2$, implying $B \propto V/R_s \propto t^{-1} \propto R_s^{-1/m}$ (e.g., Chevalier 1996). This is shown as the dashed line in Figure 10. Although there is formally better agreement with the $B \propto R_s^{-1}$ curve (*dotted line*), the errors in the data in Figure 10 are large enough that we find it difficult to separate these two cases. In the following discussion, we will assume that the magnetic field follows

$$B(t) = B_{10}\left(\frac{t}{10\ \mathrm{days}}\right)^{-1}\left(\frac{V_0}{2.2\times 10^4\ \mathrm{km\ s^{-1}}}\right)^4, \quad (47)$$

with $B_{10} = 34$ G. This choice is of no importance for the subsequent analysis and is only argued from the point of view of the possible importance of equipartition.

The ratio of the magnetic energy density to the thermal energy density behind the shock is

$$\frac{u_B}{u_{\rm therm}} \approx 0.14\left(\frac{B_{10}}{34\ \mathrm{G}}\right)^2 \dot{M}^{-1}, \quad (48)$$

independent of time. It is interesting that the field is of the same order as that given by equipartition. The difference from equipartition is, however, significant.

4.3. *Injection Rate of Nonthermal Electrons*

As we discuss in more detail in the next section, the power-law index of the injected electron spectrum is close to $p_i = 2.1$ and constant in time. We therefore use this value in the discussion below. In Figure 11 we show the density of the injected nonthermal electrons, given by $n_{\rm rel}$, as a function of shock radius. The value of $n_{\rm rel}$ is determined mainly by the optically thin flux and, therefore, from the arguments in § 5, can be shown to depend on velocity as $n_{\rm rel} \propto V^{3-2p_i} \propto V^{-1.2}$. A least-squares fit to the data in Figure 11 for the first 100 days is given by

$$n_{\rm rel} = n_{\rm rel\,15}\,\gamma_{\rm min}^{-1.1}\left(\frac{R_s}{10^{15}\ \mathrm{cm}}\right)^{-\eta}\left(\frac{V_0}{2.2\times 10^4\ \mathrm{km\ s^{-1}}}\right)^{-1.2}, \quad (49)$$

where $n_{\rm rel\,15} = (6.1 \pm 0.7) \times 10^4$ cm^{-3} and $\eta = 1.98 \pm 0.04$. After 100 days there is a prominent steepening of the slope, and one finds that $n_{\rm rel\,15} = (4.0 \pm 0.9) \times 10^5$ cm^{-3} and $\eta = 2.64 \pm 0.05$. A fit based on $\eta = 2$ during the first 100 days gives $n_{\rm rel\,15} = (6.4 \pm 0.8) \times 10^4$ cm^{-3}.

Chevalier (1996) has discussed scalings for the number density of relativistic particles based on either a constant fraction of the thermal particle density, $n_{\rm rel} \propto \rho_{\rm wind} \propto R^{-2}$, or a constant fraction of the thermal energy density, $n_{\rm rel} \propto \rho_{\rm wind}\ V^2 \propto R^{-2}V^2 \propto t^{-2}$. Here $\rho_{\rm wind}$ is the wind density. These scalings have little physical motivation and can only

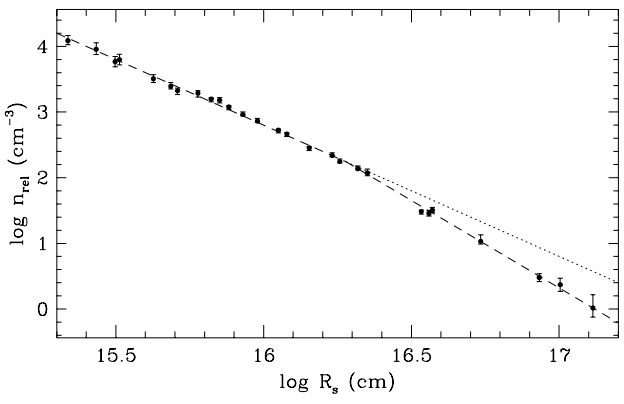

FIG. 11.—The number of relativistic particles as a function of the shock radius. The dashed line shows the expected evolution if $n_{\rm rel} \propto \rho_{\rm wind} V_s^2$, while the dotted line shows the evolution if $n_{\rm rel} \propto \rho_{\rm wind}$.

be justified by observations. An argument in favor of these scalings is that similar scalings have reproduced the light curves of other supernovae dominated by free-free absorption. We can now test these scalings directly against the observations in the same way as the magnetic field. Taking the two alternatives for the relativistic particle injection efficiencies into account, we write

$$n_{\rm rel} = f_{\rm rel} n_e \left(\frac{V}{V_0}\right)^{2\epsilon}, \quad (50)$$

where $\epsilon = 0$ for $n_{\rm rel} \propto \rho_{\rm wind}$ and $\epsilon = 1$ for $n_{\rm rel} \propto \rho_{\rm wind} V^2$. The thermal electron density, n_e, behind the shock is given by equation (16).

As long as the velocity is constant, both prescriptions give the same result, $n_{\rm rel} \propto R^{-2}$. When the velocity decreases after 100 days, $\rho_{\rm wind} V^2 \propto t^{-2} \propto R_s^{-2/m} \propto R_s^{-2.66}$ for $m = 0.74$. This is shown as the dashed line in Figure 11. As is obvious from both the figure and the fit above, $n_{\rm rel} \propto \rho_{\rm wind} V^2$ reproduces the observations remarkably well, while the $n_{\rm rel} \propto \rho_{\rm wind}$ model is incompatible with the observed evolution. This important result shows that *a fixed fraction*, $f_{\rm rel}$, of the thermal particle energy density is accelerated to relativistic energies.

The best-fit value of $f_{\rm rel}$ found by this analysis and the modeling in next section is $f_{\rm rel} = 1.85 \times 10^{-4}$. The energy density in relativistic electrons immediately behind the shock is

$$u_{\rm rel} = f_{\rm rel} n_e m_e c^2 \frac{(\gamma_{\rm min}^{-p_i+2} - \gamma_{\rm max}^{-p_i+2})}{(p_i - 2)} \equiv f_{\rm rel} n_e m_e c^2 Q(\gamma_{\rm min}, \gamma_{\rm max}, p_i) . \quad (51)$$

The ratio of the nonthermal electron density and the thermal total energy density behind the shock is $u_{\rm rel}/u_{\rm therm} \approx 5.9 \times 10^{-5} Q$. For $p_i = 2.1$, $\gamma_{\rm min} = 1$, and $\gamma_{\rm max} = \infty$, $Q = 8.7$; while $\gamma_{\rm min} = 5$ and $\gamma_{\rm max} = 15$, corresponding to the directly inferred range at 10 days, gives $Q = 0.9$. In either case the nonthermal *electron* density is much smaller than the thermal electron density, in contrast to the Razin case. There may, however, be a substantial energy density of nonthermal *ions* accelerated by the shock. For an equal number density of ions, one then gets $u_{\rm ion}/u_{\rm therm} \approx 0.11Q$. It is therefore conceivable that, to within an order of magnitude, rough equipartition between the nonthermal particles, the magnetic field and the thermal energy is present behind the shock. This conclusion rests, however, totally on the ad hoc assumption of equal efficiency for accelerating electrons and ions.

5. RADIO LIGHT CURVES FOR SN 1993J

The most direct way to compare the model with the observations is through the radio light curves at the different wavelengths. By calculating the time evolution, we can also include other effects that were not possible for the analysis above. It therefore serves as a check on the assumptions of this analysis. In contrast to the analysis in §§ 4.2 and 4.3, we now make an assumption about the behavior of the magnetic field and injection efficiency. For the injection rate we use equation (50), with $\epsilon = 0$ or $\epsilon = 1$. The high ratio of $u_B/u_{\rm therm}$ (eq. [48]) may be taken as an argument for a scaling $u_B \propto u_{\rm therm}$, or $B \propto t^{-1}$, rather than $B \propto R_s^{-1}$, and the calculations below therefore assume $B \propto t^{-1}$. As we show, the results are essentially independent of this assumption. For the radiative transfer we use equations (1), (6), and

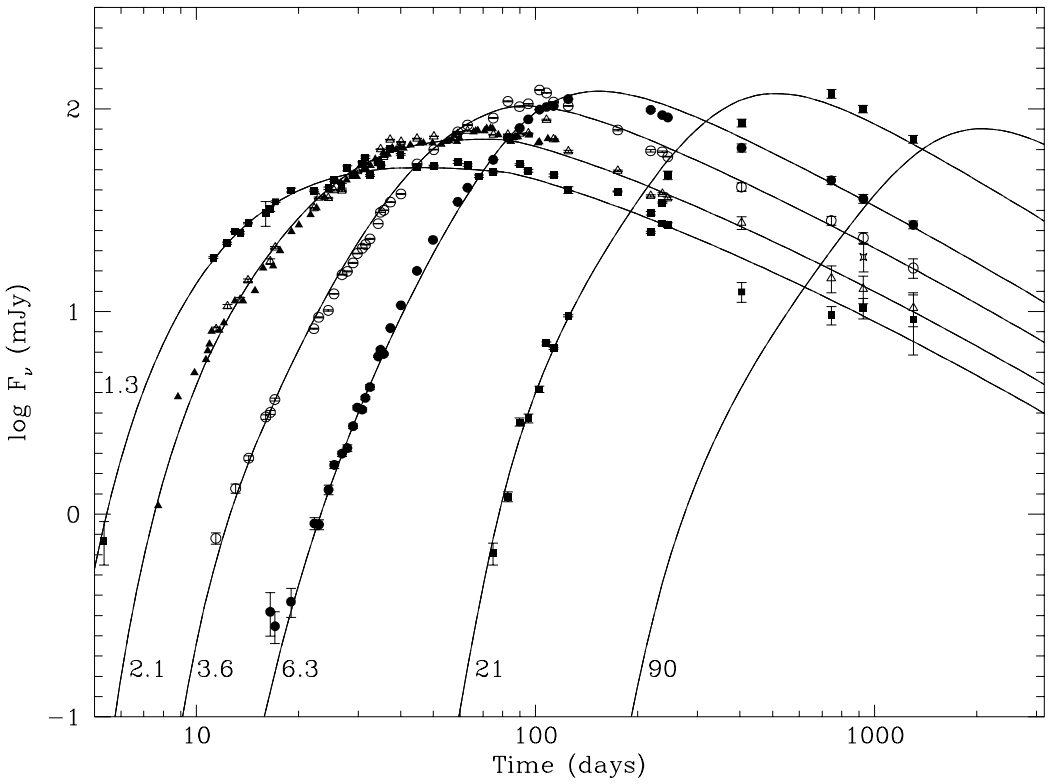

FIG. 12.—Calculated and observed radio light curves for the model with $p_i = 2.1$, $\epsilon = 1$, $f_{\rm rel} = 1.85 \times 10^{-4}$, and $n = 6.5$, discussed in the text, together with VLA observations, and the 2 cm Ryle observations (*filled triangles*).

(8). In contrast to § 4, we now use the full form of equation (40), including self-absorption effects on the electron distribution, as well as advection and the explicit time dependence.

The evolution of the velocity of the shock (through B, $n_{\rm rel}$, and R) is important for the number of relativistic electrons, and we use the parameterization in § 3.2.3. In the analysis we include all VLA observations, as well as the 2 cm observations by Pooley & Green (1993). In particular, this includes several observations from 5 to 10 days, which were not used in the analyses in §§ 3.1.2 and 4.

The resulting model light curves are shown in Figure 12, together with all observations. As can be seen, the model reproduces the light curves at the different wavelengths very well. The reproduction of the observed slope at early times is a result of

$$F_\nu(\tau_{\rm ssa} \gg 1) \propto R^2 S_\nu e^{-\tau_{\rm ff}} \propto R^2 B^{-1/2} e^{-\tau_{\rm ff}} \propto t^{2.5} e^{-\tau_{\rm ff}} \quad (52)$$

(e.g., Chevalier 1982b). This is considerably shallower than the pure free-free case discussed by FLC96. Because the magnetic field is mainly determined by the optically thick part of the spectrum, equation (52) illustrates the sensitivity of the derived value of B to the free-free optical depth.

In Figure 13 we show the electron distribution at three different epochs, and in Figure 14 we show the effective spectral index of the electron distribution, $p_{\rm eff} \equiv 2\alpha + 1$, at the energies responsible for the emission at the different observed wavelengths. At early times the range is very large, $p_{\rm eff} = 1.3$–2.5, while at $t \gtrsim 1000$ days the range is smaller at $p_{\rm eff} = 2.4$–2.8 (yet still higher than p_i), showing that cooling is important throughout the whole period. The range of $p_{\rm eff}$ even at late times clearly illustrates the necessity of doing a self-consistent calculation of the spectrum, as has been done here, rather than an analysis based on a constant spectral index as in § 3.1.2. The evolution of the electron spectrum can be compared directly with Figure 7, where it is seen that for the shortest wavelengths synchrotron cooling dominates, while at longer wavelengths Coulomb cooling dominates before $\sim$100 days, explaining the low value of $p_{\rm eff}$, especially for 21 cm. It is, however, important to note that the effects of the various cooling processes extend over a considerable energy range, and the values of $\gamma_{\rm synch}$ and $\gamma_{\rm Coul}$ are only rough indicators of the cooling effects.

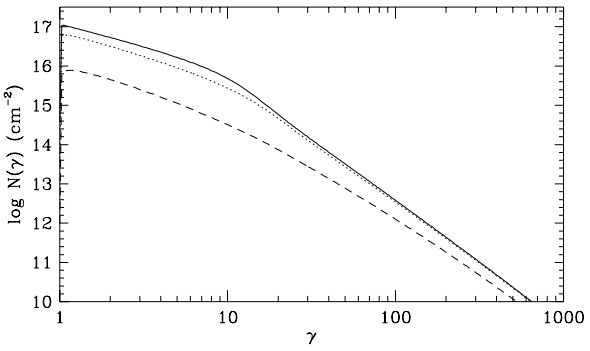

FIG. 13.—Integrated line-of-sight electron spectra at 10 (*solid line*), 100 (*dotted line*), and 1000 (*dashed line*) days. The flattening of the spectrum caused by Coulomb losses below $\gamma \sim 10$ is evident at especially 10 and 100 days, while above this energy synchrotron losses prevail. At 10 days synchrotron self-absorption heating gives a weak bump in the spectrum at $\gamma \sim 10$, corresponding to the energy of the electrons at which the optical depth is larger than one.

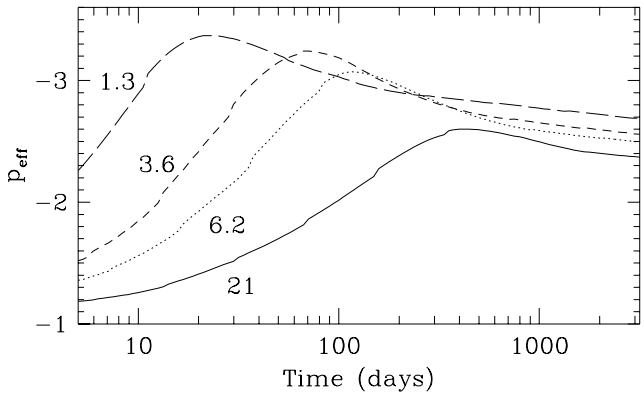

FIG. 14.—The effective spectral index $p_{\rm eff}$ of the electron distribution at the Lorentz factor [$\gamma = 85(B\lambda)^{-1/2}$] responsible for the emission at 1.3–21 cm for the model in Fig. 12.

Synchrotron self-absorption effects on the electron distribution are modest and can be seen only close to the peak in the spectrum (Fig. 13). This is the cause of the crossing of the spectral index curves seen in Figure 14. The reason for the modest self-absorption effects on the electrons is that the Coulomb timescale is shorter than the synchrotron timescale for γ corresponding to $\tau(\nu) \gtrsim 1$. The electrons are therefore downscattered in energy faster than they are redistributed by the self-absorption, in agreement with what de Kool et al. (1989) find. The optically thick flux is quite independent of assumptions about spectral index or cooling, which are important when $\tau_s \lesssim 1$. Only close to the peak in the spectrum, where $\tau_s \sim 1$, can some effects of the self-absorption on the electron distribution be seen.

Free-free optical depth unity is reached on days 12.6, 26, and 80 for 3.1, 6.2, and 21 cm, respectively. At the shorter wavelengths it never exceeds unity because of the high circumstellar temperature. The Razin effect is unimportant for the flux at all wavelengths because of the necessarily high magnetic field.

Both the optically thin luminosity and the optical depth are determined by the line-of-sight integrated number of relativistic electrons per energy, $N(\gamma)$, and a qualitative discussion of this quantity is of interest. For this purpose we neglect the self-absorption effects on the electron spectrum, as well as the Razin suppression. If we write equation (43) in terms of the synchrotron timescale $t_{\rm synch} = 6\pi m_e c/\sigma_{\rm T}\gamma B^2$, we get

$$N(\gamma) = \frac{dn}{d\gamma}\Delta R_{\rm em} = \frac{3\pi m_e c V n_{\rm rel}}{2\sigma_{\rm T} B^2 \gamma_{\rm min}^2}\left(\frac{\gamma}{\gamma_{\rm min}}\right)^{-(p_i+1)} \times \left[1 + C(t) + \left(\frac{\gamma_{\rm s\text{-}C}}{\gamma}\right)^2 + \frac{1.0}{\gamma}\left(\frac{B_{10}}{30\ {\rm G}}\right)^{-2}\left(\frac{t}{10\ {\rm days}}\right)\right]^{-1}, \quad (53)$$

where

$$C(t) = 2.49 \times 10^{-2}\left(\frac{B_{10}}{30\ {\rm G}}\right)^{-2}\left(\frac{L_{\rm Bol}(t)}{10^{42}\ {\rm ergs\ s^{-1}}}\right) \times \left(\frac{V}{2 \times 10^4\ {\rm km\ s^{-1}}}\right)^{-2}. \quad (54)$$

The term $C(t)$ gives the ratio of inverse Compton to synchrotron losses and can in our case be neglected. The third term in the bracket gives the Coulomb to synchrotron losses (eq. [39]), and the last, the adiabatic losses. When synchrotron losses dominate, the factor $\gamma^{-(p_i+1)}$ means that the integrated electron spectrum is steepened by one power, while if Coulomb losses dominate, it is flattened by one.

Using equations (53), divided by 4π, and a delta function approximation for the total emissivity of a single electron in an isotropic magnetic field, $j(\gamma, \nu) = c\sigma_T B^2\gamma^2\delta(\nu - \nu_0 B\gamma^2)/6\pi$ and $j_\nu \Delta R_{\rm em} = \int N(\gamma)/4\pi j(\gamma, \nu)d\gamma$, in equation (5) with $\bar{\tau}_{\rm ff} \ll 1$, we find

$$F_\nu(\tau_{\rm ssa} \ll 1) = \frac{1}{4}\left(\frac{R_s}{D}\right)^2 m_e c^2 V n_{\rm rel} \gamma_{\rm min}^{p_i-1} \times (\nu_0 B)^{(p_i-2)/2}\nu^{-p_i/2}\left[1 + C + \frac{\nu_{\rm Coul}}{\nu}\left(\frac{t}{10\ \rm days}\right)^{-1} + \left(\frac{\nu_{\rm ad}}{\nu}\right)^{1/2}\left(\frac{t}{10\ \rm days}\right)^{1/2}\right]^{-1}, \quad (55)$$

where

$$\nu_{\rm Coul} = 9.32 \times 10^9\left(\frac{B_{10}}{30\rm G}\right)^{-1}\mathscr{M}\left(\frac{V}{2 \times 10^4\ \rm km\ s^{-1}}\right)^{-2}\ \rm Hz\ , \quad (56)$$

$$\nu_{\rm ad} = 1.25 \times 10^8\left(\frac{B_{10}}{30\ \rm G}\right)^{-3}\ \rm Hz\ . \quad (57)$$

With equations (16), (47), and (50), we get

$$F_\nu(\tau_{\rm ssa} \ll 1) = 1.41 \times 10^8 f\dot{\mathscr{M}}\left(\frac{B_{10}}{30\ \rm G}\right)^{p_i/2-1} \times \left(\frac{V_0}{2 \times 10^4\ \rm km\ s^{-1}}\right)\left(\frac{1.26 \times 10^8}{\nu}\right)^{p_i/2} \times \left(\frac{t}{10\ \rm days}\right)^{-(2\epsilon+1)(1-m)-(p_i-2)/2} \times \left[1 + C(t) + \frac{\nu_{\rm Coul}}{\nu}\left(\frac{t}{10\ \rm days}\right)^{-1} + \left(\frac{\nu_{\rm ad}}{\nu}\right)^{1/2}\left(\frac{t}{10\ \rm days}\right)^{1/2}\right]^{-1}\ \rm mJy\ . \quad (58)$$

The slow increase in the flux of the optically thin light curves at 1.3 and 2 cm before 100 days is caused by the decreasing importance of Coulomb losses with time. Furthermore, taking $\alpha = d\ln F_\nu/d\ln\nu$ in equation (58) and using $p_{\rm eff} = 2\alpha + 1$ gives a good representation of the evolution of the electron spectral index at the various wavelengths, as shown in Figure 14.

After $\sim$100 days the shock velocity decreases according to $m \approx 0.74$. Neglecting the variation in the denominator of equation (58) (in brackets), we get for $\gtrsim$100 days $F_\nu(\tau_{\rm ssa} \ll 1) \propto t^{-0.31-0.52\epsilon}$. The evolution of the optically thin flux is therefore considerably steeper if $\epsilon = 1$, $F_\nu(\tau_{\rm ssa} \ll 1) \propto t^{-0.83}$, compared with $\epsilon = 0$. Comparing with the observations after $\sim$100 days there is much better agreement with the $n_{\rm rel} \propto \rho_{\rm wind} V^2$ model, compared with the $n_{\rm rel} \propto \rho$ model. The $n_{\rm rel} \propto \rho_{\rm wind}$ model gives too slow a decline for reasonable values of p_i and m. This is consistent with the conclusions in § 4.3. We also note the insensitivity of the optically thin flux to the magnetic field when $p_i \approx 2$, $F_\nu \propto B^{(p_i-2)/2}$, explaining the difficulty of separating the $B \propto R^{-1}$ and $B \propto t^{-1}$ cases.

The break in the light curves at $\sim$100 days occurs in our models because of the decrease in velocity, rather than as a result of a transition to the adiabatic phase. The rather abrupt change in the light curves, as well as in $n_{\rm rel}$ in Figure 11, shows that the transition from constant velocity to a more rapid decrease is fairly sharp, and should reflect a similarly well-defined flattening in the ejecta structure.

For our parameters adiabatic cooling starts to dominate at $t \sim 1000$ days. However, as can be seen from Figure 14, the spectral index even at 3000 days is considerably higher than the input spectral index, $p_i = 2.1$. In the adiabatic phase the optically thin flux scales as

$$F_\nu(\tau_{\rm ssa} \ll 1) \propto t^{-(p_i-1)/2-(1+2\epsilon)(1-m)}\ . \quad (59)$$

We have also experimented with different slopes of the injection spectrum, p_i. The most sensitive part of the spectrum is not surprisingly the epoch later than $\sim$100 days, when most of the spectrum is optically thin. At these epochs the light curves are quite sensitive to p_i, and variations in the range $2.0 \lesssim p_i \lesssim 2.2$ change the fit to the light curves markedly (as shown by the χ^2_ν). Our conclusion is therefore that the spectral index of the injected electrons should be in the above range, and not be changing in time. A value $p_i = 2.1$ is remarkably close to what diffusive shock acceleration gives, although it is not obvious why other acceleration mechanisms, like turbulent acceleration behind the shock, should give the same result.

Another conclusion is that we can check the validity of the approximate equation (43) for the electron spectrum compared with the full solution of equation (40). We find that the difference between these approaches is small in both the magnetic field and nonthermal electron density. This is illustrated by the fact that our approximate analytical solutions (52) and (58) accurately describe the numerical light curves. The results in § 4 should therefore not be affected by the additional effects included in this section.

6. FREE-FREE ABSORPTION, SYNCHROTRON SELF-ABSORPTION, AND THE RAZIN EFFECT FOR RADIO SUPERNOVAE

One may ask under what circumstances free-free absorption, synchrotron self-absorption, or the Razin effect will be important. This is discussed extensively from the point of view of different supernova categories by Chevalier (1998). Here we limit ourselves to a few supplemental remarks. The radial optical depth to free-free absorption is

$$\tau_{\rm ff} \approx 4.2\lambda^2\dot{\mathscr{M}}^2\left(\frac{T_e}{10^5\ \rm K}\right)^{-3/2}\left(\frac{V}{2 \times 10^4\ \rm km\ s^{-1}}\right)^{-3} \times \left(\frac{t}{10\ \rm days}\right)^{-3}\ . \quad (60)$$

In the synchrotron cooling domain, and assuming for simplicity that $p_i = 2$, the synchrotron optical depth is $\tau_s \approx$

$1.6 \times 10^4 f_{\rm rel} \dot{\mathscr{M}} (B_{10}/30\ {\rm G})^{1/2} (V/2 \times 10^4\ \ {\rm km}\ \ {\rm s}^{-1})^{-1} (t/10$ days$)^{-5/2} \lambda^{7/2}$. From this we note that τ_s in this case is fairly insensitive to the magnetic field. In the adiabatic regime we get $\tau_s \approx 1.9 \times 10^5 f_{\rm rel} \dot{\mathscr{M}} (B_{10}/30{\rm G})^2 (V/2 \times 10^4\ {\rm km\ s}^{-1})^{-1}$ $(t/10\ {\rm days})^{-3} \lambda^3$. In accordance with our results in § 4.2, we further assume that the magnetic field is some fraction ϕ of the equipartition value, $B_{10} \approx 1 \times 10^2 \phi^{1/2} \dot{\mathscr{M}}$ G. The ratio of the synchrotron self-absorption and free-free optical depths is then in the cooling case

$$\frac{\tau_s}{\tau_{\rm ff}} \approx 6.7 \times 10^3 f_{\rm rel} \phi^{1/4} \dot{\mathscr{M}}^{-3/4} \left(\frac{T_e}{10^5\ {\rm K}} \right)^{3/2} \times \left(\frac{V}{2 \times 10^4\ {\rm km\ s}^{-1}} \right)^2 \left(\frac{t}{10\ {\rm days}} \right)^{1/2} \lambda^{3/2}\ , \quad (61)$$

and in the adiabatic case

$$\frac{\tau_s}{\tau_{\rm ff}} \approx 4.8 \times 10^5 f_{\rm rel} \phi \left(\frac{T_e}{10^5\ {\rm K}} \right)^{3/2} \left(\frac{V}{2 \times 10^4\ {\rm km\ s}^{-1}} \right)^4 \lambda\ . \quad (62)$$

With the same assumptions, the ratio of the synchrotron cooling time to the expansion time is

$$\frac{t_{\rm synch}}{t} \approx 1.1 \times 10^{-2} \phi^{-3/4} \dot{\mathscr{M}}^{-3/2} \left(\frac{t}{10\ {\rm days}} \right)^{1/2} \lambda^{1/2}\ . \quad (63)$$

Unless $\dot{\mathscr{M}} \ll 1$ and/or $\phi \ll 1$, synchrotron cooling is likely to be important.

Equation (61) shows that in the cooling case (1) free-free absorption decreases in importance with time relative to synchrotron self-absorption, and (2) that, while insensitive to the magnetic field, the ratio is highly sensitive to the velocity and temperature of the circumstellar medium.

The magnetic field is probably related to the progenitor system, and may differ between normal Type II, IIb, and Ib supernovae. Because the latter types are likely to be components in binary systems, this fact may influence the circumstellar magnetic field. In addition, the turbulent amplification behind the shock may depend on the properties of the shock (e.g., whether it is cooling or not). Because of the lack of knowledge of this quantity it is fortunate that the optical depth is not very sensitive to the magnetic field.

The circumstellar temperature is especially sensitive to the expansion velocity, since this, together with the mass loss rate, determines the shock temperature, and therefore also the EUV and soft X-ray flux from the supernova (Lundqvist & Fransson 1988). A higher expansion velocity leads to a higher shock temperature and a stronger UV and soft X-ray spectrum from Comptonized radiation and thereby to a higher circumstellar temperature. Observationally, both SN 1993J and SN 1994I (Filippenko et al. 1995) had higher expansion velocity ($\gtrsim 2 \times 10^4$ km s^{-1}) than SN 1979C and SN 1980K ($\sim 1.2 \times 10^4$ km s^{-1}). In addition, the color temperature of the initial burst of the supernova is higher for a compact progenitor, like for a Type Ib/c or IIb supernova, which increases the heating of the circumstellar medium further. The difference in the supernova properties is illustrated in the different circumstellar temperatures found for SN 1979C and 1980K, compared with SN 1993J. In the former cases Lundqvist & Fransson (1988) found a peak temperature of $\sim 2 \times 10^5$ K, while in the latter case the peak temperature was $\gtrsim 10^6$ K (FLC96). Even more important, at 100 days the temperature was still $\sim 2 \times 10^5$ K for SN 1993J, while it was only (2–3) $\times 10^4$ K for SN 1979C and SN 1980K.

Therefore, equations (61) and (62) show that a higher expansion velocity increases the importance of synchrotron self-absorption relative to free-free absorption both directly and through the temperature.

One should note that even if synchrotron self-absorption is larger than free-free, the rise of the light curve may be dominated by the free-free, since this acts externally to the synchrotron emitting region. Because $\tau_{\rm ff}$ itself is so sensitive to the velocity and temperature (eq. [60]), the sensitivity to the velocity and progenitor structure is still present. The relative importance of synchrotron self-absorption and free-free absorption may therefore mainly be a result of the higher expansion velocity for the Type IIb and Ib/c supernovae compared with ordinary Type II supernovae.

For objects that are dominated by free-free absorption, equation (61) gives rise to the question whether synchrotron self-absorption may be important for the underlying spectrum also in these sources. Because of the limited number of observed frequencies this question is difficult to answer, although the above estimates makes this plausible.

That a high expansion velocity is indicated for the supernovae showing synchrotron self-absorption has been argued earlier by Shklovskii (1985) and more recently by Chevalier (1998). These authors have discussed especially the radio emission from the Type Ib supernovae and conclude that the expansion velocities of these indeed have to be very high. The sensitivity to the temperature has, however, been discussed little before.

As was illustrated in § 3.1.1, the main problem for the Razin effect to be important is that it requires a very low magnetic field. To give a detectable radio emission, it then follows that the column density of relativistic particles has to be unrealistically high. The high thermal plasma density needed for the Razin effect to dominate also means that Coulomb losses will become important. We therefore do not expect the Razin effect to be very important for supernovae showing an observable radio emission in other than quite exceptional cases.

7. GENERAL CONSEQUENCES FOR VLBI OBSERVATIONS

Both the dominance of the synchrotron self-absorption and the importance of electron energy losses have consequences for the VLBI observations. At wavelengths $\lambda \gg \lambda_{\tau_{\rm ssa}=1}$ the intensity will be that of a uniform disk, while at $\lambda \ll \lambda_{\tau_{\rm ssa}=1}$ limb brightening is important (Marscher 1985). For this latter situation the full set of equations (1)–(3) should be used. Free-free absorption with the consequent limb darkening is only important for the longest wavelengths. VLBI observations by Bartel et al. (1994) and Marcaide et al. (1997) have been obtained at 1.35 and 2.01 cm from day 30 to day 91, at 3.56 cm from day 50 to day 427, and at 6.16 cm from day 91 to day 1304. We find that the synchrotron optical depth is larger than unity up to day 16, 32, 63, and 125 at 1.35, 2.01, 3.56, and 6.16 cm, respectively. At times earlier than these epochs a uniform disk is therefore to be preferred as input to the VLBI modeling, while a limb-brightened shell is more applicable after these epochs.

Synchrotron losses have been shown to be important throughout the whole period of observations. If acceleration takes place close to the circumstellar shock in a very

thin region, the emitting region will have a wavelength-dependent thickness

$$\Delta R \approx \frac{V t_{\rm synch}}{4} \propto V B^{-3/2} \lambda^{1/2} . \quad (64)$$

In this ideal case the thickness would therefore increase with wavelength by a factor of $\sim 40\%$ from 3 to 6 cm. One would also predict that the thickness would increase with time as the synchrotron timescale increases (Fig. 7). If the acceleration process takes place in the turbulent region behind the shock, possibly connected to the contact discontinuity, a more uniform emissivity would result. As long as synchrotron cooling dominates, the emissivity is not sensitive to the magnetic field distribution, because the flux is instead determined by the available energy in relativistic electrons. The opposite is true if the electrons are adiabatic.

For the wavelengths where the supernova is optically thick to synchrotron self-absorption, one expects the polarization to be low, while in the optically thin phase the polarization can be high, unless the magnetic field is highly random. Because of the high degree of spherical symmetry, the integrated polarization is likely to be low. VLBI polarization maps would therefore be highly interesting although difficult to obtain in practice. A few resolution elements over the disk would suffice for this purpose.

8. CONCLUSIONS

Here we summarize our main conclusions:

1. The light curves are characterized by synchrotron self-absorption in combination with external free-free absorption. While giving an excellent fit to the spectrum, the Razin effect can be excluded, based on an unrealistic injection efficiency.

2. The circumstellar density is consistent with a constant mass-loss rate and wind velocity, $\rho_{\rm wind} \propto r^{-2}$.

3. The free-free absorption inferred from the combined synchrotron-self absorption plus free-free model agrees well with that estimated previously by FLC96.

4. The magnetic field in the synchrotron emitting region can be reliably determined, and decreases like $B \propto R_s^{-1}$, or alternatively as $B \propto t^{-1}$. The strength argues strongly for turbulent amplification behind the shock. The energy density is somewhat weaker than equipartition, $u_B/u_{\rm therm} \approx 0.14$.

5. Both synchrotron and Coulomb losses are important for the integrated electron spectrum, which cannot be characterized by a simple power law.

6. The injected electron spectrum has a power-law slope $p_i = 2.1$, indicating that diffusive shock acceleration is operating.

7. The number density of relativistic electrons scales as a fixed fraction of the thermal energy density behind the shock. This may argue for an injection mechanism that is controlled by the available thermal energy behind the shock. While the energy density in the relativistic electrons is only $\sim 5 \times 10^{-4}$ of the thermal energy density, the ions may have a total energy density comparable to equipartition.

8. The light curves, as well as the evolution of the injection rate of relativistic electrons, reflect the dynamics of the shock wave and therefore also the ejecta structure.

We are grateful to Lewis Ball, Dick McCray, Kurt Weiler, and especially Roger Chevalier and Peter Lundqvist for many informative and interesting discussions and to Kurt Weiler for making the VLA data publicly available. We are also grateful for many useful comments by the referee. This research was supported by the Swedish Natural Sciences Research Council and the Göran Gustafsson Foundation for Research in Natural Sciences and Medicine. Part of this work was done while C. F. was a visitor at the Institute for Theoretical Physics at the University of California at Santa Barbara Institute, supported by NSF under grant PHY 94-071194.

REFERENCES

Ball, L., & Kirk, J. G. 1992, ApJ, 396, L39
Bartel, N., et al. 1994, Nature, 368, 610
Chang, J. S., & Cooper, G. 1970, J. Comp. Phys., 6, 1
Chevalier, R. A. 1982a, ApJ, 258, 790
———. 1982b, ApJ, 259, 302
———. 1984, Ann. NY Acad. Sci., 422, 215
———. 1990, in Supernovae, Ed. A. G. Petschek (Berlin: Springer), 91
———. 1996, in ASP Conf. Ser. 93, Radio Emission from the Stars and the Sun, ed. A. R. Taylor & J. M. Parades (San Francisco: ASP), 125
———. 1998, ApJ, in press
Chevalier, R. A., Blondin, J. M., & Emmering, R. T. 1992, ApJ, 392, 118
Chevalier, R. A., & Dwarkadas, V. V. 1995, ApJ, 452, L45
Cohen, R. J., et al. 1987, MNRAS, 225, 491
de Kool, M., Begelman, M. C., & Sikora, M. 1989, ApJ, 337, 66
Duffy, P., Ball, L., & Kirk, J. G. 1995, ApJ, 447, 364
Filippenko, A. V., et al. 1995, ApJ, 450, L11
Fransson, C. 1994, in Circumstellar Media in the Late Stages of Stellar Evolution, ed. R. E. S. Clegg, I. R. Stevens, & W. P. S. Meikle (Cambridge: Cambridge Univ. Press), 120
———. 1998, in preparation
Fransson, C., Lundqvist, P., & Chevalier, R. A. 1996, ApJ, 461, 993 (FLC96)
Freedman, W. L., et al. 1994, ApJ, 427, 628
Jun, B., & Norman, M. L. 1996, ApJ, 472, 245
Lewis, J. R., et al. 1994, MNRAS, 266, L27
Lundqvist, P. 1994, Circumstellar Media in the Late Stages of Stellar Evolution, ed. R. E. S. Clegg, W. P. S. Meikle, & I. R. Stevens (Cambridge: Cambridge Univ. Press), 213
Lundqvist, P., & Fransson, C. 1988, A&A, 192, 221
Marcaide, J. M., et al. 1995a, Nature, 373, 44
———. 1995b, Science, 270, 1475
Marcaide, J. M., et al. 1997, ApJ, 486, L31
Marscher, A. P. 1985, in Supernovae as Distance Indicators, ed. N. Bartel (Berlin: Springer), 130
McCray, R. 1969, ApJ, 156, 329
Montes, M. J., Kassim, N. E., Weiler, K. W., Sramek, R. A., & Van Dyk, S. D. 1995, IAU Circ. 6273
Nedoluha, G. E., & Bowers, P. F. 1992, ApJ, 392, 249
Pacholczyk, A. G. 1970, Radio Astrophysics (San Francisco: W. H. Freeman)
Parker, E. N. 1958, ApJ, 128, 664
Phillips, J. A., & Kulkarni, S. R. 1993a, IAU Circ. 5775
———. 1993b, IAU Circ. 5884
Pooley, G. G., & Green, D. A. 1993, MNRAS, 264, L17
Radford, S., Neri, R., Guilloteau, S., & Downes, D. 1993, IAU Circ. 5768
Razin, V. A. 1960, Radiofiz., 3, 584
Rees, M. J. 1967, MNRAS, 137, 429
Richmond, M. W., Treffers, R. R., Filippenko, A. W., Paik, A. Y., Leibundgut, B., Schulman, E., & Cox, C. V. 1994, AJ, 107, 1022
Shigeyama, T., Suzuki, T., Kumagai, S., Nomoto K., Saio, H., & Yamaoka, H. 1994, ApJ, 420, 341
Shklovskii, I. S. 1985, Soviet Astron. Lett., 11, 105
Simon, M. 1969, ApJ, 156, 341
Slysh, V. I. 1990, Soviet Astron. Lett., 16, 339
Tsytovich, V. N. 1951, Vestn. Mosk. Univ. Phys., 11, 27

Van Dyk, S. D., Weiler, K. W., Sramek, R. A., Rupen, M. P., & Panagia, N. 1994, ApJ, 432, L115
Weber, E. J., & Davis, L., Jr. 1967, ApJ, 148, 217
Weiler, K. W., Montes, M. J., Van Dyk, S. D., Sramek, R. A., & Panagia, N. 1998, in Proc. of the Workshop SN 1987A: Ten Years After, ed. M. Phillips & N. Suntzeff (San Francisco: ASP), in press
Weiler, K. W., Sramek, R. A., Panagia, N., van der Hulst, J. M., & Salvati, M. 1996, ApJ, 301, 790
Young, T. R., Baron, E., & Branch, D. 1995, ApJ, 449, L51